Principles of energy extension in electron-emission holography

S. Y. Tong, Hua Li, and H. Huang
Department of Physics and Laboratory for Surface Studies, University of Wisconsin-Milwaukee, Milwaukee, Wisconsin 53201
(Received 2 August 1991)

We have derived the principles of energy extension in image reconstruction of electron-emission holography. We illustrate these principles with examples based on multiple-scattering simulations. The physical origins of small-window characteristics in forward-scattering and backscattering geometries are explained. We show that images reconstructed from backscattering holograms in the energy range 150–300 eV are split for the Ni(001) (1×1)-Cu system, and a method is introduced to remove this splitting. We provide a direct view of a system in which the adsorbate atom occupies an off-centered site. We discuss the energy range and optimal energy grid used in the small-window energy-extension process in the forward-scattering and backscattering geometries.

I. INTRODUCTION

Electron-emission holography as a direct structural tool has attracted a great deal of attention recently because of its potential capability for imaging single atoms in the surface and interface regions with atomic resolution.[1–6] However, unlike optical holography, the outgoing electrons are scattered strongly by the atomic potentials of the material. This strong interaction has two consequences: (i) the images are shifted from the correct atomic positions,[5] and (ii) large multiple-scattering effects are present in most systems.[7] To remedy consequence (i), methods are introduced to remove this phase shift from the emission holograms before image reconstruction.[5,8–10] Consequence (ii) is harder to overcome. Recent studies have shown that Fourier transformation (with phase-shift correction) works only in systems where single scattering dominates.[5,11] In non-single-scattering systems, image reconstruction using a single-energy hologram is unreliable: The images have poor resolution and artifacts from reconstruction are present making it difficult to identify the atomic positions.[7,8]

To overcome multiple-scattering effects, schemes are proposed to use holograms at multiple energies. Early energy-extension schemes involve adding intensities of real-space images.[12] This approach is inefficient because intensity sums cumulate reconstruction artifacts. We have proposed[8] and demonstrated[7] an energy-extension scheme for the forward scattering (FS) geometry. In our scheme, a small angular window (Ω_c: $\theta=0,\theta_c$; $\phi=0,2\pi$) is used. The small-window energy-extension process (SWEEP) joins together holograms at different energies with a different phase factor e^{ikR_0}, where R_0 is the emitter-scatterer bond length determined from a two-dimensional contour plot $\phi_{R_i}(R)$ [see Sec. II, Eq. (16)]. Here, R_i is a trial bond length and R is the Fourier variable *measured along the emitter-scatterer direction* (i.e., *focusing direction*).

The first demonstration of a multienergy phase-locking scheme is carried out in the FS geometry, using the SWEEP with $\theta_c=40°$ for a Cu(111) slab.[7,8] Full multiple-scattering calculations are used to simulate the holograms and the SWEEP method produces satisfactory results: The nearest-neighbor distance R_0 in Cu(111) is determined to within ±0.3 Å and the image has a resolution, along the focusing direction, of better than 1 Å.[7] We define image resolution as the full width at half maximum (w = FWHM) of the radial intensity scan along the emitter-scatterer direction.

In this paper, we derive and illustrate the general principles of phase-locking energy-extension schemes in the FS and backscattering (BS) geometries.[7,8,13] Because single-energy holographic image reconstruction methods fail in many systems, a multienergy process is a necessity. In the FS geometry with electron energy ≥ 200 eV, the scattering factor decays rapidly away from the forward focusing direction. In systems with multiple focusing directions,[14–18] the interference fringes usable for image reconstruction of an atom or atoms in a particular direction are limited to within an effective angular cone Ω_{eff} much smaller than the full $\Omega_{2\pi}$ hemispherical window. By introducing a small angular cone Ω_c centered at a focusing direction, we work with those interference fringes relevant to a specific atom or chain of atoms in that direction. This process reduces artifacts and it produces brighter images. We generally expect that the SWEEP method applies to the FS geometry.[7,8] In this paper, we shall show that contrary to expectation, effective small windows also exist for BS holograms. In Sec. III, we demonstrate and explain this rather unexpected result. We shall show that the principles of the SWEEP are applicable to both the FS and BS geometries.

We shall also show that atomic images reconstructed from single-energy or multienergy holograms in the 100–400-eV range are often split and a remedy is proposed to eliminate it. The BS multiple-energy process is demonstrated with multiple-scattering simulations for two systems: monolayer (1×1) Cu on Ni(001) and Ni(001)-$c(2\times2)$S. In Sec. IV, we show atomic images for a system in which the adsorbate atom occupies an off-centered site on the surface. We anticipate that the

determination of adsorption site is an important use of this technique; Sec. IV presents a direct view of these results. In Sec. V, we introduce an improvement in the determination of the bond distance in the FS geometry. The significance of choosing energy points with evenly spaced wave numbers is discussed in Sec. VII. Section VII contains a summary.

II. CHARACTERISTICS OF THE SMALL-WINDOW ENERGY-EXTENSION PROCESS

As discussed in the Introduction, a small, effective angular window often dominates the emission holograms in both FS and BS geometries. In this section, we derive and explain the characteristic of the small-window effect.

We start with the three-dimensional (3D) Fourier transformation of diffraction patterns at energy E_n,[7,8] with $k_n=\sqrt{(2m/\hbar^2)E_n}$:

$$\phi_n(\mathbf{R})=|T_n(\mathbf{R})| \tag{1}$$

$$=\left|\int \chi(k_n\hat{\mathbf{k}})\delta(k-k_n)e^{ik_n\hat{\mathbf{k}}\cdot\mathbf{R}}d^3k\right| . \tag{2}$$

Using $d^3K=k^2dk\,d\Omega$ and integrating out the δ function in Eq. (2), we obtain

$$T_n(\mathbf{R})=\int \chi(k_n\hat{\mathbf{k}})e^{ik_n\hat{\mathbf{k}}\cdot\mathbf{R}}k_n^2d\Omega . \tag{3}$$

The normalized diffraction function $\chi(k_n\hat{\mathbf{k}})$ is given by[8,19]

$$\chi(k_n\hat{\mathbf{k}})\propto\sum_\alpha\frac{|F_D(k_n,\hat{\mathbf{R}}_\alpha)|^2|f(k_n,\hat{\mathbf{k}}\cdot\hat{\mathbf{R}}_\alpha)|^2}{|F_D(k_n,\hat{\mathbf{k}})|^2R_\alpha^2}+\sum_\alpha\frac{F_D(k_n,\hat{\mathbf{R}}_\alpha)f(k_n,\hat{\mathbf{k}}\cdot\hat{\mathbf{R}}_\alpha)e^{i(k_nR_\alpha-k_n\hat{\mathbf{k}}\cdot\mathbf{R}_\alpha)}}{F_D(k_n,\hat{\mathbf{k}})R_\alpha}+\text{c.c.}+\cdots . \tag{4}$$

The first sum in Eq. (4) corresponds to the self-image terms;[7,8,20,21] the second sum corresponds to single-atom image terms at $\mathbf{R}_\alpha$.

Phase locking involves summing over a discrete set of energies with a particular phase factor.[7,8,13] Consider N energy points, in ascending order of magnitude, with wave numbers $k_1,\ldots,k_N$. For an atom at $\mathbf{R}_0$, a generalized energy-extended image function can be written as

$$\Phi_{R_i}(\mathbf{R})=\mathcal{D}\left|\sum_{n=1}^{N}e^{-ik_nR_i}T_n(\mathbf{R})\right| , \tag{5}$$

where $\mathcal{D}=(k_N-k_1)/(N-1)$ defines a mean wave-number interval and R_i is a scalar which defines the phase that joins together single-energy Fourier transforms $T_n(\mathbf{R})$. By substituting $T_n(\mathbf{R})$ from Eq. (3) and using $k_n^2d\Omega=dk_{n,\parallel}/\cos\theta$, we obtain

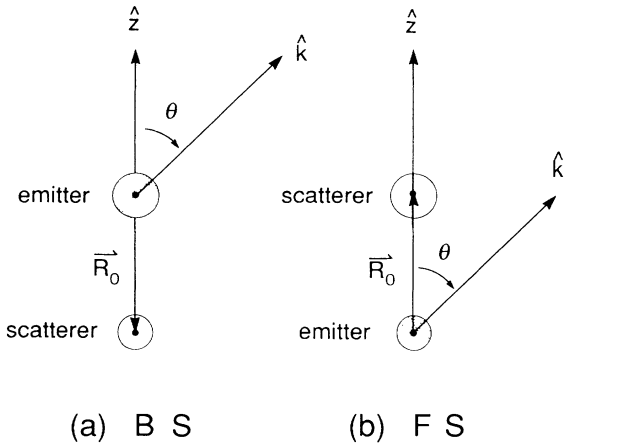

FIG. 1. Schematic diagram of emitter-scatterer system for (a) backscattering and (b) forward-scattering geometries.

$$\Phi_{R_i}(\mathbf{R})=\mathcal{D}\left|\sum_{n=1}^{N}\int\chi(k_n\hat{\mathbf{k}})e^{-ik_nR_i}e^{ik_n\hat{\mathbf{k}}\cdot\mathbf{R}}k_n^2d\Omega\right| \tag{6}$$

or

$$\Phi_{R_i}(\mathbf{R})=\mathcal{D}\left|\sum_{n=1}^{N}\int\frac{\chi(k_n\hat{\mathbf{k}})e^{-ik_nR_i}e^{ik_n\hat{\mathbf{k}}\cdot\mathbf{R}}}{\cos\theta}dk_{n,x}dk_{n,y}\right| . \tag{7}$$

A justification for Eq. (5) is that when the variable R_i equals R_0, the phase factor cancels the conjugate phase in the image term of Eq. (4) for that atom, thereby, leaving only a plane-wave phase $e^{-ik_n\hat{\mathbf{k}}\cdot\mathbf{R}_0}$ for all energies. Therefore, after performing the Fourier transform (FT) by Eq. (6) or Eq. (7), the contribution from each energy coherently cumulates at the image point $\Phi_{R_0}(\mathbf{R}_0)$, giving the desired result. Also, since the image term in Eq. (4) is only for single scattering, the sum in Eq. (5) reinforces the single-scattering contribution to the image and reduces (by phase cancellation) the multiple-scattering terms. While the maximum value of $\Phi_{R_i}(\mathbf{R})$ should occur at $R_i=R_0$ and $\mathbf{R}=\mathbf{R}_0$, the image half-width w depends on the functional dependence of R_i. The optimal functional form of R_i depends on the geometry used, FS or BS, and on whether the effective angular range is small window or full window.

To determine the optimal form of R_i, it is simplest to reduce the system to two atoms. In Sec. IV, we shall apply these results to multiatomic slab systems. Here, we consider an emitter at the origin and a scatterer at $\mathbf{R}_0$ along the z axis. For FS, the scatterer is above the emitter; for BS, the reverse is true [see Figs. 1(a) and 1(b)]. Evaluating Eq. (6) for $\mathbf{R}$ along the z axis only and explicitly writing out the image term of Eq. (4), we obtain

$$\Phi_{R_i}^{L}(R)\propto\mathcal{D}\left|\sum_{n=1}^{N}\int_0^{2\pi}\int_0^{\theta_c}\frac{e^{-ik_nR_i}e^{i(k_nR_0\mp k_nR_0\cos\theta)}e^{ik_nR\cos\theta}}{R_0}k_n^2\sin\theta\,d\theta\,d\phi\right| , \tag{8}$$

where the $-$ ($+$) sign is for the forward-scattering (backscattering) geometry and θ_c is the available polar range. In Eq. (8), we have neglected all angular and energy dependencies of the source terms such as $F_D(\hat{\mathbf{k}})$ and $F_D(\hat{\mathbf{R}}_0)$ and of the scattering factor $f(\hat{\mathbf{k}}\cdot\hat{\mathbf{R}}_0)$. The full dependencies will be restored in the actual multiple-scattering slab calculations presented in Sec. IV. Integrating out $d\phi$, we obtain

$$\Phi^I_{R_i}(R)\propto\frac{2\pi\mathcal{D}}{R_0}\left|\sum_{n=1}^{N}k_n e^{ik_n(R_0\mp R_0+R-R_i)}\left[\frac{1-e^{-ik_n(R\mp R_0)(1-\cos\theta_c)}}{(R\mp R_0)}\right]\right| . \tag{9}$$

In the small-window limit $\theta_c\approx 0°$ we can expand $(1-\cos\theta_c)$ in a power series to obtain

$$\Phi^I_{R_i}(R)\to\frac{2\pi\mathcal{D}}{R_0}(1-\cos\theta_c)\left|\sum_{n=1}^{N}k_n^2 e^{ik_n(R_0\mp R_0+R-R_i)}\left[1-\frac{i}{2}k_n(R\mp R_0)(1-\cos\theta_c)\right.\right.$$
$$\left.\left.-\tfrac{1}{6}k_n^2(R\mp R_0)^2(1-\cos\theta_c)^2+\cdots\right]\right| . \tag{10}$$

In the two-dimensional contour map of the image function $\Phi^I_{R_i}(R)$, the function varies slowly when the exponent in Eq. (10) is zero. This occurs along the line $R_i=R$ for FS and the line $R_i=2R_0+R$ for BS. Along these two lines, the function $\Phi^I_{R_i}(R)$ has the following form (to achieve this form, we convert the sum over energies into an integral over k):

$$\Phi^I_{R_i}(R)\to\frac{2\pi}{R_0}(1-\cos\theta_\alpha)\times\left[\frac{k^3}{3}[1-0.03k^2(R\mp R_0)^2\times(1-\cos\theta_c)^2+\cdots]\right]_{k_{\min}}^{k_{\max}} , \tag{11}$$

where $k_{\max}$ and $k_{\min}$ are the upper and lower limits of the wave numbers, respectively. The function in Eq. (11) is maximum at $R=R_0$ for FS and at $R=-R_0$ for BS; it falls off as $\Delta^2=(R\mp R_0)^2$ along the $R_i=R$ and the $R_i=2R_0+R$ lines, respectively.

Following the same derivation for the self-image term we obtain a similar expression, but R_0 does not appear and the FS-BS geometries have identical results. Thus, the high-intensity line for the self-image term is along $R_i=R$ for both FS and BS geometries. Along this line, the self-image term varies as

$$\Phi^S_{R_i}(R)\to\frac{2\pi}{R_0^2}(1-\cos\theta_c)\times\left[\frac{k^3}{3}[1-0.03k^2R^2(1-\cos\theta_c)^2+\cdots]\right]_{k_{\min}}^{k_{\max}} . \tag{12}$$

The self-image term maximum is at the origin (i.e., $R=0$) and it decreases like R^2 along the $R_i=R$ line.

We depict these small-window characteristics schematically in Figs. 2(a) and 2(b) for the BS and FS geometries, respectively. The hatched areas indicate high-intensity contours for the image and square (i.e., self-image) terms. It is easy to derive the corresponding expressions when a full window, i.e., $\theta_c=\pi/2$, is in effect. In the full-window case, Eq. (9) becomes

$$\Phi^I_{R_i}(R)\propto\frac{2\pi\mathcal{D}}{R_0}\left|\sum_{n=1}^{N}k_n e^{ik_n(R_0\mp R_0+R-R_i)}e^{-[ik_n(R\mp R_0)]/2}\frac{\sin\left\{\frac{k_n(R\mp R_0)}{2}\right\}}{(R\mp R_0)/2}\right| . \tag{13}$$

To determine the behavior of $\Phi^I_{R_i}(R)$ in Eq. (13), we cut along the $R=R_0$ line for FS and the $R=-R_0$ line for BS to obtain, respectively,

$$\Phi^I_{R_i}(R=\pm R_0)\to\frac{2\pi}{R_0}\left|\int_{k_{\min}}^{k_{\max}}k^2 e^{ik(R_0-R_i)}dk\right| . \tag{14}$$

The integral in Eq. (14) is evaluated as I_2 in Appendix A; it has a FWHM of $w_2=1.4\Gamma$, where $\Gamma=2\pi/\Delta k$. Here, $\Delta k=k_{\max}-k_{\min}$ is the range of the wave numbers in the energy-extension sum. If, instead, we cut along the $R_i=R_0$ line, we obtain from Eq. (13)

$$\Phi^I_{R_i=R_0}(R)\to\frac{2\pi}{R_0}\left|\int_{k_{\min}}^{k_{\max}}k e^{[ik(R\mp R_0)]/2}\times\frac{\sin\{k(R\mp R_0)/2}{(R\mp R_0)/2}dk\right| . \tag{15}$$

This integral, evaluated as I_3 in Appendix A, has a FWHM of $w_3=0.9\Gamma$ as a function of R. The maximum of the function $\Phi^I_{R_i}(R)$ in Eq. (13) occurs at $R_i=R=R_0$ (for FS) and $R_i=-R=R_0$ (for BS). From these points, Eqs. (14) and (15) indicate that the function decays 1.5

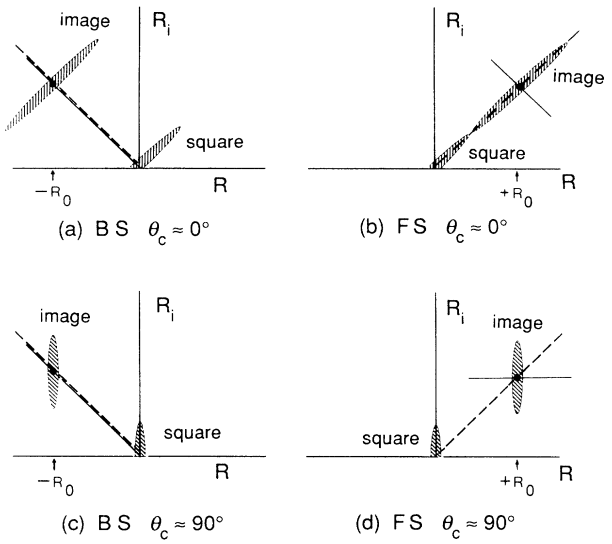

FIG. 2. High-intensity areas for the image and self-image (square) terms for small-window [(a) and (b)] and full-window [(c) and (d)] situations, respectively, in the function $\Phi_{R_i}(R)$.

times faster when R is varied (for fixed R_i), than when R_i is varied (for fixed R). Therefore, the high-intensity contours are elongated parallel to the R_i axis [see Figs. 2(c) and 2(d), respectively]. It is easy to show that for the self-image term, the maximum is at the origin; similarly, the high-intensity contours are elongated along the R_i axis.

In Figs. 2(a)–2(d), the high-intensity contours of $\Phi_{R_i}(R)$ are depicted for small (full) angular windows and forward-scattering (backscattering) geometries. These characteristics allow a systematic selection of the optimal functional form of R_i. Referring to Fig. 2, we note that to determine the bond distance R_0, one follows the line $R_i = R$ with positive R for FS and $R_i = -R$ with negative R for BS. This is true whether the angular range is full or small window. These choices are shown as broken lines in Figs. 2(a)–2(d). The maxima of $\Phi^I_{R_i}(R)$ along these lines occur at $R_i = R = R_0$ (FS) or at $R_i = -R = R_0$ (BS) with a value given by either Eq. (10) or Eq. (13) as

$$\Phi^{\max}_{R_0}(R_0) \propto \frac{2\pi}{R_0}(1-\cos\theta_c)\frac{k^3_{\max}-k^3_{\min}}{3} , \tag{16}$$

where θ_c equals $\pi/2$ for full window. Note that R_i is always positive with these choices.

With the value of R_0 determined, images are formed with the smallest w = FWHM by using the following R_i:

(a) Small window: FS $\Longrightarrow R_i = 2R_0 - R$

$$(R \geq 0);\ w \equiv 0.7\Gamma , \tag{17}$$

Full window: FS $\Longrightarrow R_i = R_0$; $w = 0.9\Gamma$ (18)

and

(b) Small window: BS $\Longrightarrow R_i = -R$

$$(R \leq 0);\ w \equiv 0.7\Gamma , \tag{19}$$

Full window: BS $\Longrightarrow R_i = -R$

$$(R \leq 0);\ w = 0.66\Gamma . \tag{20}$$

These choices of R_i correspond to cuts denoted by the solid lines in Figs. 2(a)–2(d). The values of w are the theoretical limits of the FWHM of the image and their derivations are given in Appendix A. Also, the values given in Eqs. (17) and (19) correspond to the leading term in Eq. (10); they are strictly valid if $\theta_c \Longrightarrow 0°$.

In practice, the usable angular range is somewhere between $\theta_c = 0°$ and $\pi/2$ and there is an energy dependence to this effective angular cone. Since the difference between Eqs. (17) and (18) or between (19) and (20) is small to being with, it is simpler in actual cases to use the choice $R_i = R_0$ for the FS geometry and $R_i = -R$ (where $R \leq 0$) for the BS geometry. Both these choices guarantee that the energy-dependent phase factor $e^{ik_n(R_0 \mp R_0 + R - R_i)}$ in Eq. (9) will cancel artifacts and enhance the single-scattering image at the $R = \pm R_0$ region for FS and BS geometries, respectively.

III. BACKSCATTERING GEOMETRY: THE CASE FOR SMALL WINDOW

Having derived the characteristics of small- and full-window image reconstructions we shall illustrate these properties with actual examples. Since a number of dynamical factors can cause artifacts and shifts in the reconstructed image, we use numerical simulations with increasing complexity. We start with a simple two-atom backscattering system: a Ni emitter placed at the origin and a Ni scatterer at $\mathbf{R}_0 = 2.52$ Å in the $-z$ direction. We consider the single-scattering $\chi(k_n\hat{\mathbf{k}})$ expression given in Eq. (4), which includes the c.c. term. Seventeen energies in the range of 60 to 286 eV are used; the energies are chosen so that the wave-number interval $\Delta k = k_{i+1} = \mathcal{D}$ is uniform. As noted earlier, the use of a uniform Δk produces a periodic $\Phi_{R_i}(R)$ with respect to R_i, and the period is given by $L = 2\pi/\mathcal{D}$.[7,8] In this case the period is $L = 21.4$ Å. This period is very large, and it ensures that in the region of interest no artifacts are present from the periods of the image and self-image. The reason for the use of a large period will be discussed in Sec. VII.

For this two-atom case, we assume once again that $F_D(\hat{\mathbf{k}})$ and $F_D(\hat{\mathbf{R}})$ in Eq. (4) are independent of energy of or angle. However, actual scattering factors calculated with plane-wave incidence are used:

$$f(k_n, \hat{\mathbf{k}}\cdot\hat{\mathbf{R}}_0) = \frac{1}{2ik_n}\sum_{l=1}^{N}(2l+1)P_l(\hat{\mathbf{k}}\cdot\hat{\mathbf{R}}_0)(e^{2i\delta_{l,k_n}}-1) . \tag{21}$$

In Eq. (21), $P_l(\hat{\mathbf{k}}\cdot\hat{\mathbf{R}}_0)$ is the Legendre polynomial and δ_{l,k_n} is the lth partial-wave phase shift at wave number k_n. For comparison with this model, we also perform similar simulations, but the scattering factor is set to a constant: $f = R_0$. The functions $\chi(k_n, \hat{\mathbf{k}})$ are evaluated according to Eq. (4); the two-dimensional function $\Phi_{R_i}(R)$ is gen-

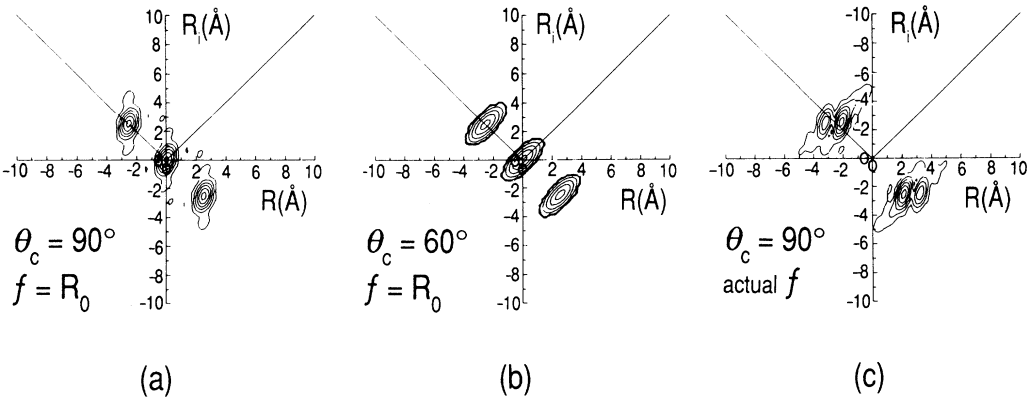

FIG. 3. High-intensity contours of $\Phi_{R_i}(R)$ for a diatomic Ni system. The image is at $R=-2.52$ Å, the self-image at $R=0$, and the twin at $R=2.52$ Å. Using actual back scattering factors the image is split [panel (c)].

erated according to Eq. (6) with R_i and R measured along the emitter-scatterer direction (i.e., $\pm z$ axis).

We show in Figs. 3(a)–3(c) the high-intensity contours of $\Phi_{R_i}(R)$ for this two-atom system. In Fig. 3(a), a full window $\theta_c=\pi/2$ and $f=R_0$ are used. The high-intensity contours are elongated parallel to the R_i axis, in accordance with the full-window backscattering behavior depicted in Fig. 2(c). The image and self-image appear in the positive R_i half plane; their corresponding twins appear in the negative R_i half plane. The constant $f=R_0$ scattering factor ensures that the usable range of the diffraction equals the window opening (i.e., $\theta_c=\pi/2$). Figure 3(b) shows the contours as the opening window is decreased to $\theta_c=60°$. The high-intensity contours rotate and point towards 45° lines, in accordance with the predictions of Fig. 2(a). Figure 3(a) shows the contours for a full opening window, $\theta_c=\pi/2$, where actual calculated backscattering factors $f(k_n,\hat{\mathbf{k}}\cdot\hat{\mathbf{R}}_0)$ according to Eq. (21) are used in $\chi(k_n\hat{\mathbf{k}})$. One notices two unexpected results: (i) The high-intensity contours are elongated towards 45°, reflecting a small-window character even though a full opening window is used, and (ii) the image (and twin) shows a splitting in intensity. We now provide the reasons for these results.

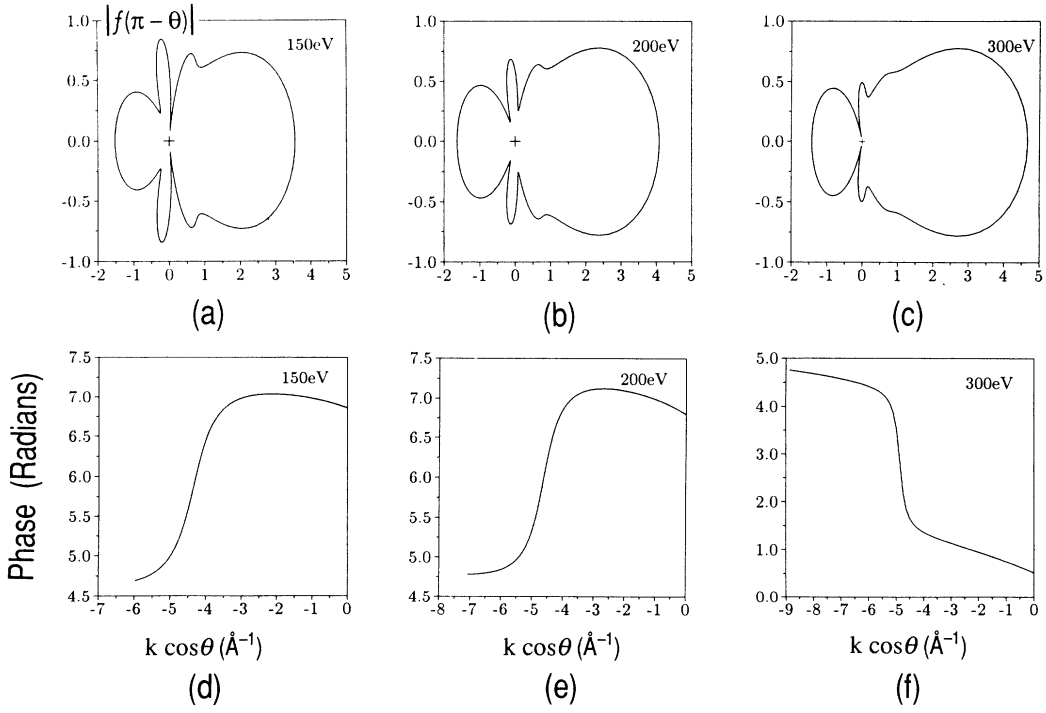

FIG. 4. The magnitude [(a)–(c)] and phase [(d)–(f)] of the backscattering factor at 150, 200, and 300 eV. In (a)–(c), $\pi\geq\theta\geq\pi/2$ are along negative abscissa values, and $\pi/2\geq\theta\geq 0$ are along positive abscissa values. The phase in (d)–(f) is shown for $\pi\geq\theta\geq\pi/2$ values.

A. Origin of split peaks

The origin of the splitting in the energy-extended image must be due to the Ni backscattering factor $f(k_n, \hat{\mathbf{k}}\cdot\hat{\mathbf{R}}_0)$ since there is no splitting if a constant $f=R_0$ is used. To investigate further, we plot in Figs. 4(a)–4(c) the magnitude $|f(\pi-\theta)|$ at three typical energies in this range: 150, 200, and 300 eV, respectively. In these figures, $f(0°)$ is forward scattering and $f(\pi)$ is backscattering. We notice strong angular anisotropies in $|f(\pi-\theta)|$, especially the sharp cusps at which the magnitude of $|f|$ almost vanishes. At the cusps, the phase of $f(\pi-\theta)$ goes through a near π resonance, as shown in Figs. 4(d)–4(f). The sharp cusps and π change in the phase of $f(\pi-\theta)$ cause image peaks to be split (see longer discussion given in Appendix B). This effect has also been observed by Barton *et al.*[22] to cause peak splittings in the Fourier transformation of energy-dependent photoemission fine-structure spectra. From the behavior of $f(\pi-\theta)$ at these energies, we expect the images reconstructed from the individual energies to be split also. This is indeed the case, as shown in Figs. 5(a)–5(c) where the image intensity is plotted from the origin (i.e., emitter position) along the $-z$ direction. All three images are split. The correct image position, at $R=-2.52$ Å, is marked by an arrow. It falls between the split peaks. For each doublet, the higher intensity peak is caused by the part of the scattering factor which ranges from π to the cusp at 120°–135°. The slope of the phase in this angular region is positive at 150 and 200 eV [see Figs. 4(d) and 4(e), respectively], while it is negative at 300 eV [Fig. 4(f)]. At backscattering, the image is phase shifted according to $R\approx -R_0+b$, where b is the slope. This means that at 150 and 200 eV, the higher intensity peak of the doublet is shifted towards the origin, while at 300 eV, it is shifted towards larger negative values. These trends are reflected in the image doublets shown in Figs. 5(a)–5(c). At 400 eV or above, the cusp in $|f(\pi-\theta)|$ becomes less deep, the slope of the phase remains negative, but the sharp π resonance disappears. The single-energy reconstructed image is no longer split at 400 eV or above, but the peak is shifted towards larger negative R.

The splitting in the image peak is most pronounced in the 150–350-eV range for Ni, exactly the energy range best suited for holographic reconstruction in the BS geometry. This is unfortunate because a split image from single-energy or multienergy reconstruction causes large uncertainties in the structural determination. In Sec. III B, we shall propose a way to overcome this problem.

B. Origin of the small-window character in backscattering

The deep cusps in the Ni $|f(\pi-\theta)|$ which cause image peaks to become split also are responsible for the small-window characteristics of $\Phi_{R_i}(R)$. Referring to Fig. 5, the image doublet is caused by reconstruction functions which use separate (small) angular regions of the diffraction fringes, therefore, the image behaves as if the opening is much less than $\pi/2$. Because the backscattering factor $f(\pi-\theta)$ introduces an effective small angular window, we can use the small-window energy-extension process to improve the image resolution.

To demonstrate improvement in the image resolution by the SWEEP, we show the energy-extended images for the three cases of Fig. 3. We evaluate $\Phi_{R_i}(R)$ according to Eq. (6) with R varying from 0 to -6 Å along the z axis and we put $R_i=-R$ in the phase factor $e^{-ik_n R_i}$. The radial image intensity scans are shown in Figs. 6(a)–6(c), respectively. For comparison, we show in Figs. 6(d)–6(f) similar scans for the images reconstructed from the largest energy (i.e., $E=286$ eV). The FWHM of each case is indicated. Comparing the full-window case, i.e., Figs. 6(a) and 6(d), the width w is the same to two decimal places. This is because at the largest energy, the width is given by $w_1\simeq 2.4k_{\max}^{-1}$ (see Appendix A). The width for the full-window energy-extended image is given by Eq. (20), i.e., $w_2\simeq 1.3\pi(k_{\max}-k_{\min})^{-1}$. With the energies used, $E_{\max}=286$ eV and $E_{\min}=60$ eV, the two quantities w_1 and w_2 are almost identical. It is possible to improve resolution with full-window energy extension, but $E_{\min}$ has to be small (e.g., in this case, $E_{\min}$ must be less than 58 eV; see condition derived in Appendix A).

It is, however, much easier to improve resolution if the effective window θ_c is less than $\pi/2$. We show this in Figs. 6(b) and 6(e) or in Figs. 6(c) and 6(f). The widths for the energy-extended images improve by 47% and 28%,

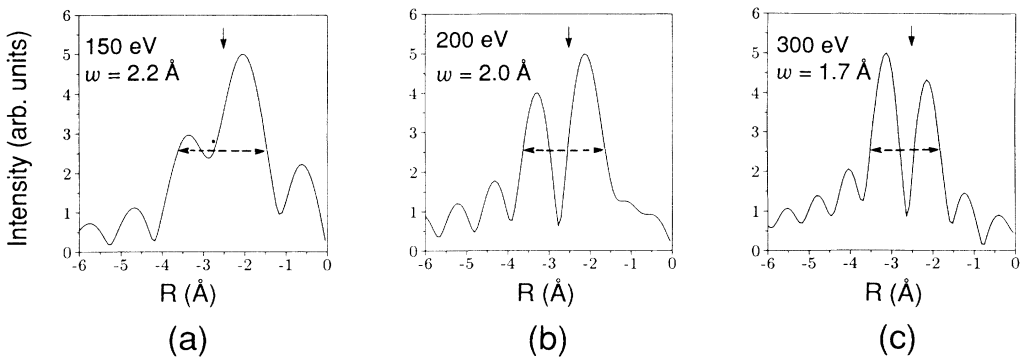

FIG. 5. Radial image intensity plots with emitter at the origin and scatterer at $R=-2.52$ Å (arrow). The images are split due to cusps in the backscattering factor; w is the FWHM.

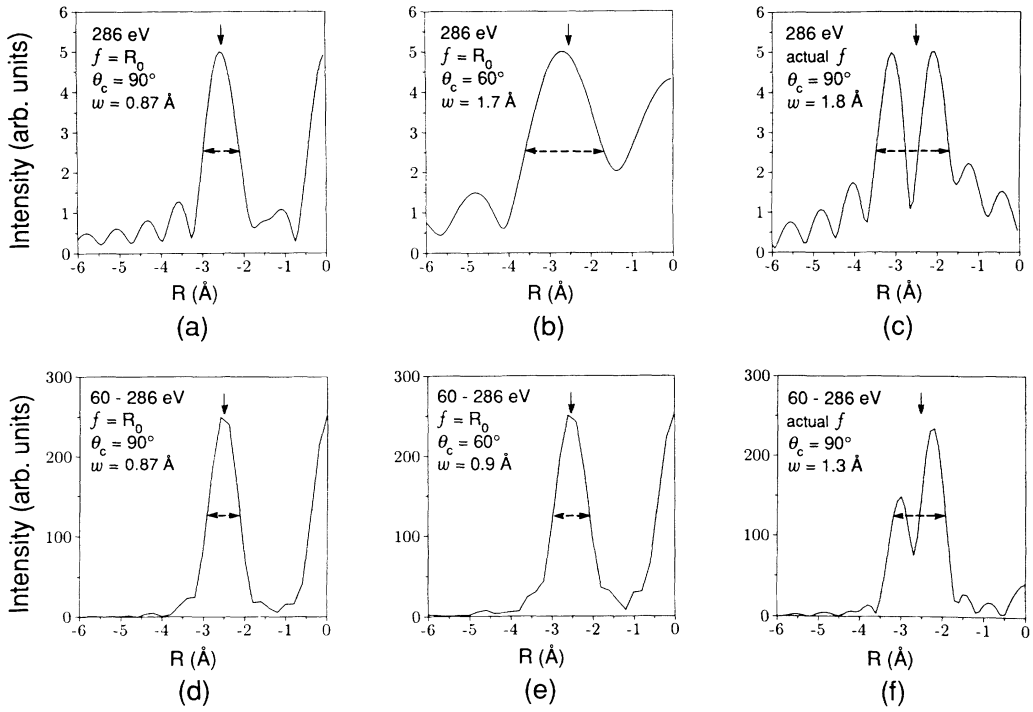

FIG. 6. Radial image intensity plots with emitter at origin and scatterer at $R=0.252$ Å (arrow) for single-energy [(a)–(c)] and energy-extended [(d)–(f)] cases, respectively.

respectively, depending on $f(\theta)$ and the size of the effective window. Another way to understand the improvement in the image resolution is to consider the schematic diagram shown in Fig. 7. Here, multiple k_i are chosen so that no gap exists in Δk_z. This is ensured if $k_{i+1} \leq k_i/\cos\theta_c$. Referring to this figure, the wave-number range at the highest energy is given by

$$\Delta k_z = k_5 - k_5\cos\theta_c \ . \tag{22}$$

By energy extension, a new range is obtained:

$$\Delta k_z(\text{SWEEP}) = k_5 - k_1\cos\theta_c \tag{23a}$$

or

$$\Delta k_z(\text{SWEEP}) = k_5 - k_5\cos\theta_n \ . \tag{23b}$$

As long as $\theta_c \ll \pi/2$, either due to a dynamical factor [e.g., $f(\pi-\theta)$] or an actual small collection window, then we have $\Delta k_z(\text{SWEEP}) \gg \Delta k_z$ because k_1 is smaller than k_5. Since the image resolution is inversely proportional to the wave-number range, the resolution is *always* improved by energy extension in the BS geometry for small-window situations.

We are now in a position to remedy the split peaks in the energy-extension result. Since we realize that the higher intensity peak in the doublet is due to the back-scattering lobe of $|f(\pi-\theta)|$, we can limit $\chi(k_n\hat{\mathbf{k}})$ to a small window. In Fig. 8(a), we show the image intensity plot reconstructed from the highest energy, with $\theta_c = 60°$. The peak splitting is eliminated, but the resolution is rather poor, with $w = 2.7$ Å. However, with the same energy-extension process as before, but with θ_c reduced to 60°, we improve the resolution to $w = 1.15$ Å [Fig. 8(b)]. A shoulder, instead of a split peak, is formed, while the highest peak is at -2.3 Å, which is 0.22 Å away from the correct position. With θ_c further reduced to 45° [Fig. 8(c)], a single peak, essentially symmetrical, is formed at the correct position.

We would like to stress the central idea behind the SWEEP. In the presence of dynamical or physical factors which limit the usable data range, using a full window does not improve accuracy, it simply increases artifacts. If we compare the single-energy full-window [Fig. 6(c)] and small-window [Fig. 8(a)] results for an identical system, the full window leads to split peaks, which generates wrong conclusions. In using a small window, noise and artifacts are eliminated, leading to a more accurate image position whose resolution can then be improved

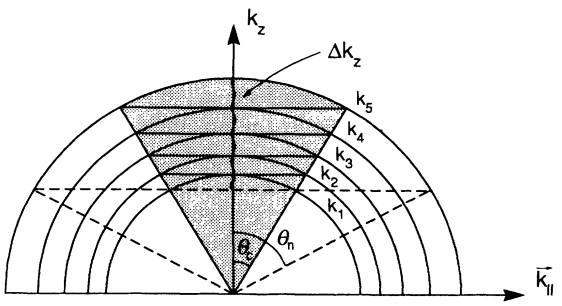

FIG. 7. Illustration of Δk_z extension (wiggly line) for a small-window $\theta_c < \pi/2$. The angular window is enlarged to θ_n after the 5 energy extensions.

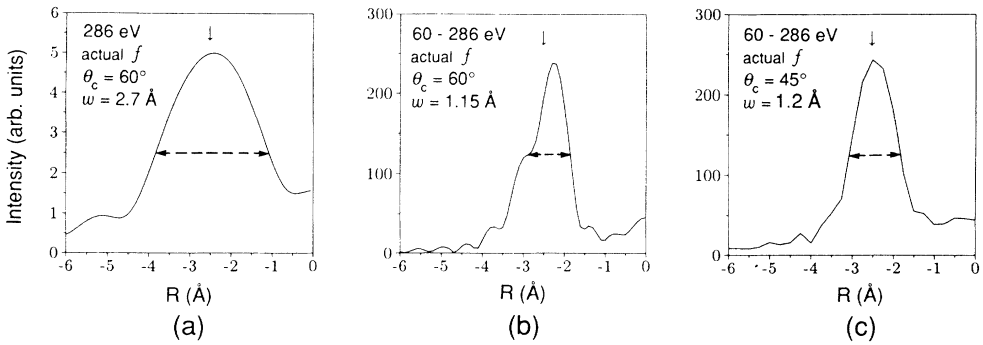

FIG. 8. Small-window radial image intensity plots with single-energy [(a)] and energy-extended [(b) and (c)] cases, respectively. The emitter is at the origin and the scatterer at $R=-2.52$ Å (arrow).

through energy extension. In actual applications in the BS geometry, a full window is first used to locate the general areas of the images. If an image is split or the noise level around it is high, a small angular cone centered along the particular emitter-image direction is applied and the SWEEP is carried out using the $\chi(k_n\hat{\mathbf{k}})$ in that cone only. This process can be repeated for images in other directions. An example of this procedure is given in the next section.

IV. BACKSCATTERING ENERGY EXTENSION FOR Ni(001) (1×1)-Cu AND Ni(001) $c(2\times2)$-S

We now apply the principles derived in Sec. II to two realistic systems: an ordered monolayer of Cu on Ni(001) and $c(2\times2)$S on Ni(001). The approximations applied in earlier examples are lifted; in particular, a fully dynamical multiple-scattering slab method is used to calculate emission holograms at different energies. Dynamical source terms $F_D(k_n,\hat{\mathbf{k}})$ with $s\rightarrow p$ and $p\rightarrow d,s$ transition matrix elements for the Cu($2p$) and S($1s$) core levels are evaluated at each energy.[23] The exact Green's-function structural propagators are used to evaluate the near-field (i.e., curved wave) scattering t matrices.[24,25] Approximation schemes such as the separable representation or Taylor series, magnetic-quantum-number expansion, etc. are not used.

The normalized interference function of Eq. (4) is defined as

$$\chi(k_n\hat{\mathbf{k}})=\frac{I(k_n\hat{\mathbf{k}})-I_D(k_n\hat{\mathbf{k}})}{I_D(k_n\hat{\mathbf{k}})}\ , \tag{24}$$

where $I(k_n\hat{\mathbf{k}})$ is the calculated (or measured) total intensity and $I_D(k_n\hat{\mathbf{k}})$ is the intensity of the reference wave. In a theoretical simulation, the absolute values of I and I_D are calculated. However, when I from an experimental measurement is used, the absolute intensity (per incident photon per unit area per second) is only approximately known. A simple approximation of I_D is to use the average:

$$A(k_n)=\frac{1}{\Omega_0}\int_{\Omega_0} I(k_n\hat{\mathbf{k}})d\Omega\ . \tag{25}$$

This choice of the angular average probably overestimates the actual reference wave intensity and introduces background noise in the image reconstruction; however, its appeal is in the simplicity of Eq. (25). In the examples given in this section, this simple choice is used and the normalized holograms are defined as[7,8]

$$\chi(k_n\hat{\mathbf{k}})=\frac{I(k_n\hat{\mathbf{k}})-A}{A}\ . \tag{26}$$

From the discussions in Sec. II, in the BS geometry, the use of $R_i=-R$ ($R\le 0$) in Eq. (7) forms the image as well as giving the best cut for the resolution [via Eq. (19)]. However, in the $R>0$ half plane, we have a choice. If we put $R_i=R$, we cut along the 45° direction in the first quadrant of Fig. 3(c)—the solid line. This line runs along the high-intensity streak of the self-image term for small window. Alternatively, one may choose the line $R_i=-R$ ($R>0$), which cuts through at $-45°$ in the fourth quadrant. This line passes through the twin image. Writing out these two choices explicitly by substituting them into Eq. (7), we obtain for the first choice[13]

$$\Phi(\mathbf{R})=\mathcal{D}\left|\sum_{n=1}^{N}\int\frac{\chi(k_n\hat{\mathbf{k}})e^{-ik_nR}e^{ik_n\hat{\mathbf{k}}\cdot\mathbf{R}}}{\cos\theta}dk_{n,x}dk_{n,y}\right| \quad \text{(for all } \mathbf{R}\text{)}\ . \tag{27}$$

The second choice corresponds to

$$\Phi(\mathbf{R})=\begin{cases}\mathcal{D}\left|\sum_{n=1}^{N}\int\frac{\chi(k_n\hat{\mathbf{k}})e^{ik_nR}e^{ik_n\hat{\mathbf{k}}\cdot\mathbf{R}}}{\cos\theta}\times dk_{n,x}dk_{n,y}\right| & (R_z>0) \quad (28a)\\ \mathcal{D}\left|\sum_{n=1}^{N}\int\frac{\chi(k_n\hat{\mathbf{k}})e^{-ik_nR}e^{ik_n\hat{\mathbf{k}}\cdot\mathbf{R}}}{\cos\theta}\times dk_{n,x}dk_{n,y}\right| & (R_z\le 0)\ . \quad (28b)\end{cases}$$

In the example given below, results of both choices are given.

The first example is for an ordered layer of Cu atoms

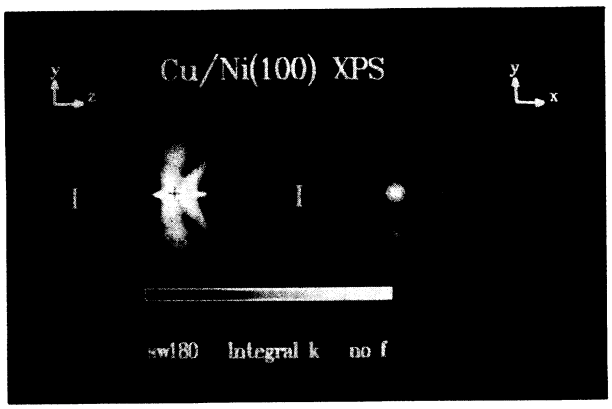

FIG. 9. Full-window ($\theta_c = 90°$) energy-extended image reconstruction using Eq. (27). Left panel: Cut normal to surface. Right panel: Cut parallel to surface. Vertical bar indicates 1 Å.

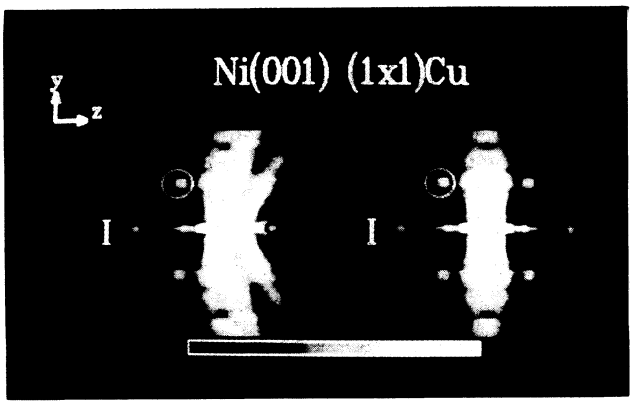

FIG. 10. Full-window ($\theta_c = 90°$) energy-extended image reconstruction. Left panel: Same as that in Fig. 9. Right panel: Cut normal to surface; Eq. (28) is used in the image reconstruction process. Vertical bar indicates 1 Å.

occupying the fourfold hollow site on Ni(001) with a Cu-Ni spacing of 1.8 Å. The energy-extension scheme uses 17 energies, from 60 to 681 eV with equally spaced wavenumber intervals. The period $L = 2\pi/\mathcal{D}$ is 10.7 Å. In Fig. 9, we show the energy-extended image reconstruction results. The choice of R_i is according to Eq. (27). The left side shows a plane normal to the surface passing through the Cu emitter (marked by a cross) and two nearest-neighbor Ni atoms (marked by circles) as well as a next-nearest-neighbor Ni atom directly below the Cu atom. The images of the two nearest Ni neighbors are 2.38 Å from the origin (correct distance is 2.52 Å, error $= 0.15$ Å). The image FWHM is 0.69 Å. The images are not split because we have extended the energy to 681 eV. The image of the next-nearest-neighbor Ni atom directly below the Cu atom is at 3.25 Å (correct distance is 3.56 Å, error $= 0.31$ Å).

On the $+z$ side, the high-intensity noise is very evident. This is because Eq. (27) follows the 45° line in the first quadrant of Fig. 3(c) and this line runs parallel to the high-intensity streak of the self-image term. In a slab geometry, there are many Ni scatterers and they all contribute to the self-image term [see Eq. (4)]. In Fig. 3(c), the self-image term is very weak because there is only one scatterer. As pointed out earlier, we can use Eq. (28) to avoid the 45° line through the first quadrant. This result is shown in Fig. 10, right panel, where with **R** running along the emitter-scatterer direction, Eq. (28) corresponds to a line passing through the image and twin. Hence, we see a mirror symmetry, with the twins appearing in the $z > 0$ half plane. Equation (28) contains information about the twins, which become useful when phase shifts are corrected (the phase-shift correction breaks the mirror symmetry between the image and twin).[5]

The right panel of Fig. 9 shows a cut parallel to the surface at 1.8 Å below the Cu plane. This plane passes through the first-layer Ni nuclei. The image reconstruction shows four nearest-neighbor Ni atoms, whose distance from the center is 2.12 Å (correct distance is 1.76 Å, error $= 0.36$ Å).

As pointed out in the preceding section, after the approximate locations of the images are determined from a full-window reconstruction, one could use a small window to improve the image precision or remove peak splitting. The nearest- and next-nearest-neighbor images are not split with the energy range 60–681 eV used. These images become split if we reduce the range to 60–286 eV, i.e., the same range as that used in Fig. 6. The reason for the splitting has already been discussed in Sec. III. In Fig. 11, left panel, we show the split Ni images; except for the reduced energy range, all other conditions (e.g., $\Delta k = k_{i+1} - k_i$ and the period L) are identical to those used for Fig. 10, right panel. The image of the nearest-neighbor Ni atom shows a doublet, at 1.82 and 2.75 Å, respectively, compared to the correct spacing of 2.52 Å. The next-nearest-neighbor atom directly below the emitter shows a doublet at 2.60 and 3.71 Å, respectively, compared to the correct spacing of 3.56 Å. We can remove the splitting in the nearest-neighbor atom by centering a small window $\theta_c = 45°$ at a polar angle of 136° from the positive abscissa direction. The small-window image,

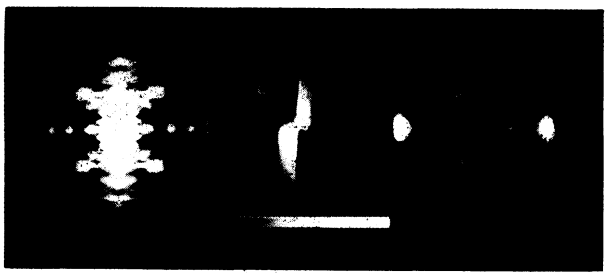

FIG. 11. Left panel: Full-window ($\theta_c = 90°$) energy-extended image reconstruction using the 60–286-eV energy range. Other conditions same as those in Fig. 10, right panel. Split images enclosed by circles. Center: Small-window ($\theta_c = 45°$) energy-extended nearest-neighbor image Crosses mark emitter and scatterer positions. Right: Small-window ($\theta_c = 30°$) energy-extended image of Ni atom below emitter. Crosses mark emitter and scatterer positions. The twin images appear on the right halves of each panel.

thus formed, is shown in Fig. 11, center panel. The small cross indicates the correct atomic position. To remove the split peaks for the image of the Ni atom directly below the Cu emitter, we use a small window $\theta_c = 30°$ centered at 180° from the positive abscissa direction. The small-window image for this Ni atom is shown in Fig. 11, right panel. Again, the small cross indicates the correct Ni atomic position. In all three panels, the twin images appear on the right halves [Eqs. (28a) and (28b) are used].

There is an alternate way to determine the atomic position, based on the fact that in the BS geometry, the self-image is elongated along the 45° line [Fig. 2(a)]; thus, we can write

$$R_s = R_i \ , \tag{29}$$

where R_s is the position of the self-image for a given R_i. The image itself is elongated along a parallel line in the second quadrant passing through R_0 [Fig. 2(a)], i.e.,

$$-R_I = 2R_0 - R_i \ . \tag{30}$$

Adding Eqs. (29) and (30), we obtain,

$$R_0 = (R_s + |R_I|)/2 \ . \tag{31}$$

Since Eq. (31) is independent of R_i, it means that the separation between the image and the self-image in a line passing through the origin is constant and equals $2R_0$. In Fig. 12, we show $\Phi_{R_i}(\mathbf{R})$ reconstructed by Eq. (7) using three trial values: $R_i = 2.22$, 2.52, and 2.82 Å, respectively. The large circles centered at the origin have radii equal to R_i, and they pass through the self-images (at the one o'clock position) according to Eq. (29). We draw a line passing through the peak of the self-image and the origin: this line cuts through the image (at the seven o'clock position). The intensity scans along this line for the three R_i values are shown in Fig. 13. From Figs. 13(a)–13(c), we obtain the average separation between the image and self-image: $D = (D_1 + D_2 + D_3)/3 = 5.14$ Å, which from Eq. (31) gives a value of $R_0 = 2.57$ Å (correct bond length is 2.52 Å, error = 0.05 Å; earlier determination of R_0 by Fig. 9 is 2.38 Å).

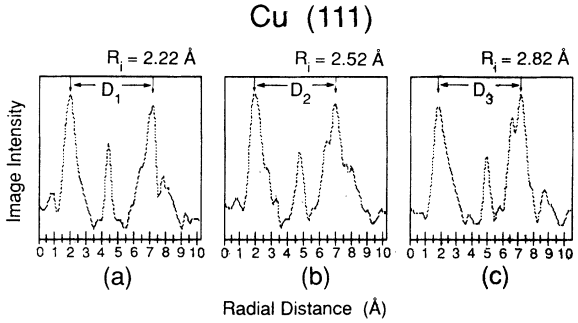

FIG. 13. Intensity scans passing through the self-image, origin, and image of Fig. 12. The peak-to-peak distance is indicated by D_i.

The conditions given in Eqs. (30) and (31) are best obeyed for $R_i \approx R_0$, hence this method could be used as a second determination of the bond length after an initial R_0 has been measured in either Fig. 9 or Fig. 11. In the BS geometry, the phase shift is not easily corrected (see Sec. VI). The self-image term is real [see Eq. (4)] and hence R_s does not depend on the phase of $f(\pi - \theta)$. This means R_0 determined by Eq. (31) contains only $\delta/2$, where δ is the shift due to the phase of the scattering factor.

We now turn to our second example: Ni(001) $c(2\times2)$-S. Thirteen energies from 60 to 452 eV are used, again with evenly spaced wave numbers. The period in $\Phi_{R_i}(R)$ is $L = 2\pi/\mathcal{D} = 10.9$ Å. Figure 14 shows Ni images from the energy-extended process where Eq. (28) is used. The (001) plane is cut parallel to the surface at 1.3 Å below the S layer. This plane passes through the nuclei of the first Ni layer. The left panel corresponds to the case where S is placed at the center of a fourfold hollow site. The cut shows the four nearest-neighbor Ni atoms at 1.94 Å from the center (correct distance is 1.76 Å, error = 0.18 Å). The right panel corresponds to S occupying an off-centered site, i.e., the S atom is displaced 0.7 Å

FIG. 12. Full-window ($\theta_c = 90°$) energy-extended image reconstruction using different trial values of R_i for the nearest-neighbor Ni atom. The separation between the self-image (at the one o'clock position) and image (at the seven o'clock position) remains constant.

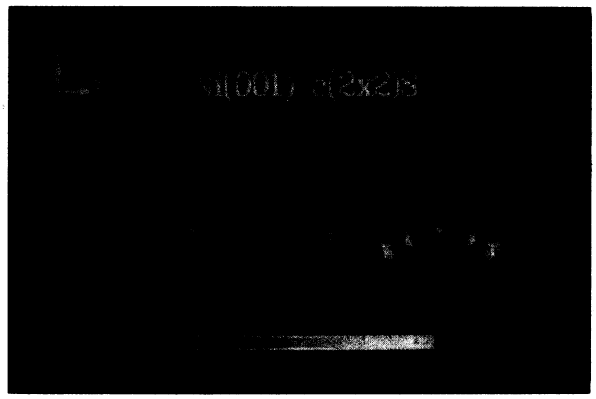

FIG. 14. Full-window ($\theta_c = 90°$) energy-extended image reconstruction for S at the symmetric fourfold site (left panel) and the asymmetric site (right panel).

in the $-\hat{\mathbf{y}}$ direction.

In this off-centered geometry, the two farther Ni neighbors are imaged at 2.37 Å (correct distance is 2.31 Å, error =0.06 Å). The two closer Ni atoms have split images—the peaks are at 0.9 Å (lower intensity) and 1.5 Å (higher intensity) from the center. If we select the higher intensity peak as the Ni image, the error is 0.14 Å (the correct distance is 1.36 Å). In an actual system, the off-centered image should be averaged over four equivalent domains. However, even summing over four 90° rotations, it is still rather easy to distinguish between the two cases—S atoms at centered off-centered sites—by direct study of the reconstructed images.

Before leaving the backscattering geometry, we point out that we are unable to produce clear-cut atomic images based on single-energy holograms, for either the Cu or S overlayer system. The failure of single-energy holograms to produce convincing images suggests that energy extension is a necessary step. The improvement is considerable, since we have started from a situation in which no recognizable image exists in the single-energy case, to the clear, highly resolved images shown in Figs. 9–11. The multiple-energy process improves resolution, and enhances the single-scattering term by adding to its intensity in a coherent fashion.

V. SMALL WINDOW IN THE FORWARD-SCATTERING GEOMETRY

In the forward-scattering geometry, $f(\theta)$ is lobed along the focusing direction at high energies (i.e., $E \geq 200$ eV) and it falls off rapidly as θ increases. However, unlike the backscattering case, there are no sharp cusps in $|f(\theta)|$ or π resonances in its phase variation, therefore by itself $f(\theta)$ does not cause the small-window situation. The small window in FS is caused by the presence of multiple focusing directions. In such systems, the diffraction fringes in a (small) angular cone around each focusing direction are dominated by the scattering of atoms situated along that particular direction. The small-window characteristics of $\Phi_{R_i}(R)$, where R is measured along a focusing direction, have high-intensity contours of the image and self-image streaked along the 45° axis in the first quadrant [see Fig. 2(b)]. These characteristics are borne out in multiple-scattering simulations of the Cu(111) slab and we refer the reader to Fig. 3 of Ref. 7 for a diagram of $\Phi_{R_i}(R)$ for R along the nearest-neighbor 35.3° focusing direction.

In using the SWEEP in the FS geometry, the first step is to determine $\mathbf{R}_\alpha$, the atomic position of the scatterer. The orientation (i.e., θ,ϕ) of $\mathbf{R}_\alpha$ can be determined from the αth focusing direction in $\mathbf{k}$ space. To determine the magnitude, we substitute $R_i = R$ in Eq. (7) and evaluate $\Phi_R^\alpha(R)$ along this focusing direction. The position of the maximum, according to Eq. (16), gives R_α. In the following, we present an improvement in the determination of R_α.

In previous works, before substituting in Eq. (7), the normalized $\chi(k_n\hat{\mathbf{k}})$ are divided by a correction function to remove the phase shift in the forward-scattering geometry.[5,7,8] The correction function has been previously defined as[8]

$$p_\alpha(k_n\hat{\mathbf{k}}) = \frac{1}{\sqrt{a}} \frac{f(k_n,\hat{\mathbf{k}}\cdot\hat{\mathbf{R}}_\alpha)}{|f(k_n,\hat{\mathbf{k}}\cdot\hat{\mathbf{R}}_\alpha)|} \sum_j |f(k_n,\hat{\mathbf{k}}\cdot\hat{\mathbf{R}}_j)| \ , \tag{32}$$

where j sums over all the focusing directions (including the αth direction) and a is the surface unit cell area introduced so that $p_\alpha(k_n\hat{\mathbf{k}})$ is dimensionless. Note that the division by $p_\alpha(k_n\hat{\mathbf{k}})$ achieves two improvements. (i) The division by a sum of $|f(\hat{\mathbf{k}}\cdot\hat{\mathbf{R}}_j)|$, each centered along a focusing direction, removes the strongly forward-peaked angular anisotropy in $\chi(k_n\hat{\mathbf{k}})$. In particular, the self-image terms in Eq. (4) are decreased, thus reducing the noise and artifacts due to these terms. (ii) The division by the phase of $f(\theta_\alpha)$ removes the position error for images along the αth focusing direction. This phase division also shifts the self-image and the twin towards the (unphysical) $-\hat{\mathbf{R}}_\alpha$ direction.[5]

An improvement to the determination of R_α can be achieved by replacing the plane wave $f(k_n,\hat{\mathbf{k}}\cdot\hat{\mathbf{R}}_\alpha)$ given by Eq. (21) with a curved-wave $f(k_n,\hat{\mathbf{k}}\cdot\hat{\mathbf{R}}_\alpha,R_\alpha)$. The first-order curved-wave correction is given by[26]

$$f(k_n,\hat{\mathbf{k}}\cdot\hat{\mathbf{R}}_\alpha,R_\alpha) = \frac{1}{2ik_n} \sum_{l=1}^{N} (2l+1)P_l(\hat{\mathbf{k}}\cdot\hat{\mathbf{R}}_\alpha) \times (e^{2i\delta_{l,k_n}}-1)C_l(k_nR_\alpha) \ , \tag{33}$$

where the polynomials $C_l(k_nR_\alpha)$ are generated by

$$C_0(k_nR_\alpha)=1$$

and

$$C_{l+1}(k_nR_\alpha) = C_{l-1}(k_nR_\alpha) + \frac{(2l+1)i}{k_nR_\alpha} C_l(k_nR_\alpha) \quad (l>1) \ . \tag{34}$$

With the curved-wave (CW) correction, the function $p_\alpha(k_n\hat{\mathbf{k}})$ becomes

$$p_\alpha^{\mathrm{CW}}(k_n,\hat{\mathbf{k}}) = \frac{1}{\sqrt{a}} \frac{f(k_n,\hat{\mathbf{k}}\cdot\hat{\mathbf{R}}_\alpha,R_\alpha)}{|f(k_n,\hat{\mathbf{k}}\cdot\hat{\mathbf{R}}_\alpha,R_\alpha)|} \times \left[|f(k_n,\hat{\mathbf{k}}\cdot\hat{\mathbf{R}}_\alpha,R_\alpha)| + \sum_{j\neq\alpha} |f(k_n,\hat{\mathbf{k}}\cdot\hat{\mathbf{R}}_j)| \right] . \tag{35}$$

Note that in Eq. (35), we have introduced the curved-wave correction only to the scattering factor along the focusing direction for which images are reconstructed. This process is permutated for other focusing directions, excluding those related by symmetry.

In Fig. 15 we show $\Phi_R^\alpha(R)$ for Cu(111) along the nearest-neighbor (35.3°) focusing direction (see schematic geometry in Fig. 16). This system has been previously analyzed in which 14 energies are used with $E_1=263$ eV and $E_{14}=1836$ eV. The energies are chosen to have evenly spaced wave numbers giving a period of $L=5.96$

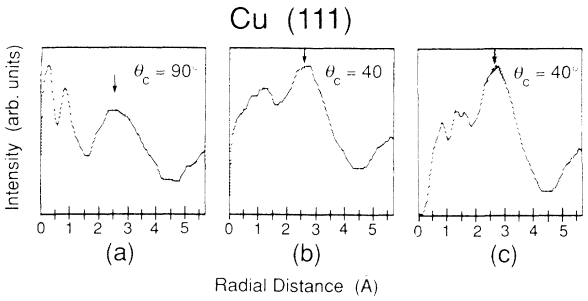

FIG. 15. Plot of $\Phi_R^{\alpha}(R)$ vs R along the nearest-neighbor 35.3° focusing direction of a Cu(111) slab. The correct Cu-Cu nearest-neighbor distance is marked by an arrow.

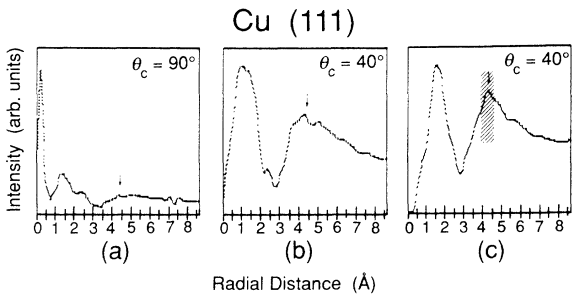

FIG. 17. Plot of $\Phi_R^{\beta}(R)$ vs R along the next-nearest-neighbor 19.5° focusing direction of a Cu(111) slab. The correct distance is marked by an arrow.

Å. In Fig. 15(a), we show $\Phi_R^{\alpha}(R)$ where a full window ($\theta_c=\pi/2$) and the plane-wave correction function given in Eq. (32) are used. Figure 15(b) uses Eq. (32) also, but a small window $\theta_c=40°$ centered along the 35.3° focusing direction is used. Figure 15(c) uses the same $\theta_c=40°$ small window and the curved-wave correction function of Eq. (35). The peak at 2.65 Å in Fig. 15(c) is most intense and sharpest compared to that in Fig. 15(a) or 15(b). The peak position of 2.65 Å±0.3 Å is compared to the correct value of 2.55 Å (error =0.1 Å). The artifacts at $R \leq 1.5$ Å are due to the self-image terms [see Fig. 2(b)] and these are smallest for Fig. 15(c). Therefore, using the curved-wave correction function to divide $\chi(k_n\hat{\mathbf{k}})$ is an improvement over using the plane-wave form. Comparing the full-window [Fig. 15(a)] and small-window [Fig. 15(b)] results, we note once again that increasing the angular window, in this case, does not improve resolution—rather, the artifacts at $R \leq 1.5$ Å increase in intensity. With a full window, all focusing directions (and hence self-images) of the system are included.

The small-window process, on the other hand, emphasizes diffraction fringes of interest and cuts out many focusing (i.e., self-image) terms. In Fig. 17, $\Phi_R^{\beta}(R)$ for Cu(111) is shown where β is the next-nearest-neighbor focusing direction (i.e., 19.5° in Fig. 16). The result using the full-window, plane-wave correction function [Fig. 17(a)] again shows the dominance of the self-image terms (at $R \leq 2$ Å). The image position R_{β} cannot be determined in this case. An appreciable improvement is obtained when a small window is used, e.g., $\theta_c=40°$ in Fig. 17(b). Finally, using $\theta_c=40°$ and a curved-wave correction function, the result in Fig. 17(c) yields $R_{\beta}=4.3\pm0.3$ Å compared to the correct value of 4.42 Å (error=0.12 Å).

In using the curved-wave function $f(k_n,\hat{\mathbf{k}}\cdot\hat{\mathbf{R}}_{\alpha},R_{\alpha})$, we need an approximate (or first determination) value of R_{α} as an input to Eq. (33). This value can be obtained from the plot in panel (b) of Fig. 15 or Fig. 17 where the plane wave $f(k_n,\hat{\mathbf{k}}\cdot\hat{\mathbf{R}}_{\alpha})$ is used. For this procedure to be valid, the function $f(k,\hat{\mathbf{k}}\cdot\hat{\mathbf{R}},R)$ must be slowly varying with respect to R. This is indeed the case, as we show in Fig. 18 the phase and magnitude of $f(k,\hat{\mathbf{k}}\cdot\hat{\mathbf{R}},R)$ where R is

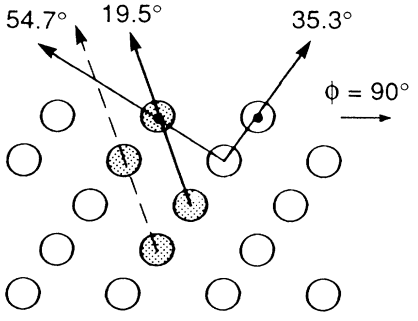

FIG. 16. Schematic Cu(111) side view showing focusing directions.

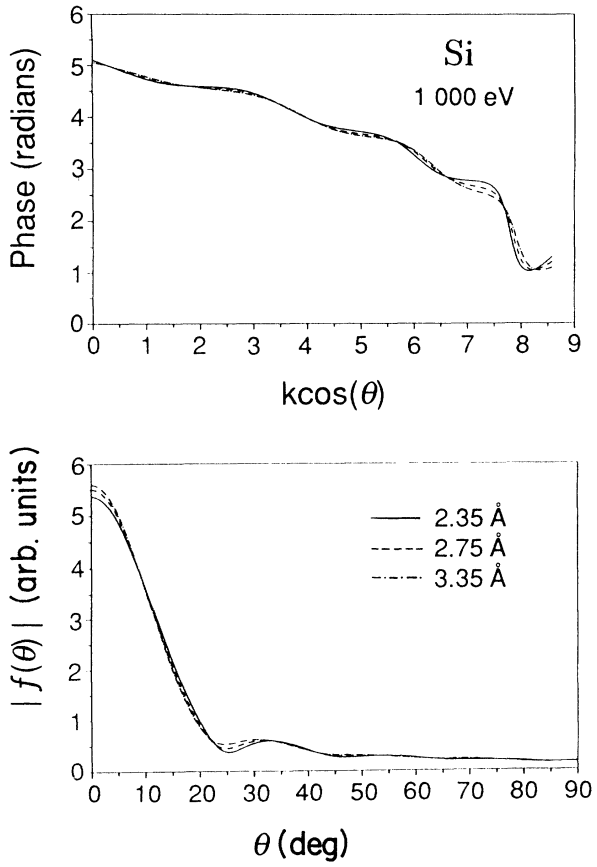

FIG. 18. The phase (upper panel) and magnitude (lower panel) of $f(k,\hat{\mathbf{k}}\cdot\hat{\mathbf{R}},R)$ for three values of R.

varied by $R=2.35$, 2.75, and 3.55 Å. We notice an extremely low sensitivity of $f(k,\hat{\mathbf{k}}\cdot\hat{\mathbf{R}},R)$ to changes of ~ 1 Å in the variable R.

The self-image artifact in Fig. 17, panel (c), is still slightly higher in intensity than the peak at 4.3 Å. One can further reduce the intensity of this artifact by either increasing the energy range or decreasing the angular window to $\theta_c=30°-35°$. After R_α is determined, we form the corresponding image by using the phase factor given in either Eq. (17) or Eq. (18). Using Eq. (17), we substitute $R_i=2R_\alpha-R$ and the phase-shift correction function into Eq. (7) to obtain[27]

$$\Phi_{R_\alpha}(\mathbf{R})=\mathcal{D}\left|\sum_{n=1}^{N}\int\frac{\chi(k_n\hat{\mathbf{k}})e^{-ik_n(2R_\alpha-R)}e^{ik_n\hat{\mathbf{k}}\cdot\mathbf{R}}}{p_\alpha(k_n\hat{\mathbf{k}})\cos\theta}dk_{n,x}dk_{n,y}\right| . \tag{36}$$

Similarly, if we use Eq. (18), we substitute $R_i=R_\alpha$ into Eq. (7) and obtain[7,8]

$$\Phi_{R_\alpha}(\mathbf{R})=\mathcal{D}\left|\sum_{n=1}^{N}\int\frac{\chi(k_n\hat{\mathbf{k}})e^{-ik_nR_\alpha}e^{ik_n\hat{\mathbf{k}}\cdot\mathbf{R}}}{p_\alpha(k_n\hat{\mathbf{k}})\cos\theta}dk_{n,x}dk_{n,y}\right| . \tag{37}$$

Along the $\hat{\mathbf{R}}$ parallel to $\hat{\mathbf{R}}_\alpha$ direction, the integrals in Eqs. (36) and (37) correspond to lines (a) and (b), respectively (see Fig. 19), which cut across the high-intensity contours of $\Phi_{R_i}(R)$ at the narrow cross sections. More importantly, either cut, (a) or (b), avoids the self-image artifacts near the origin which become strong in multiscatterer systems. Images formed by such a cut, e.g., line (b), have been obtained for the nearest- and next-nearest-neighbor atoms of Cu(111).[7]

Finally, we demonstrate that images reconstructed from single-energy holograms are of poor quality in systems such as Cu(111) where multiple-scattering effects are strong. Figures 20(a) and 20(b) show radial intensity plots along the 19.5° focusing direction for images reconstructed from single-energy holograms. The image position of 4.42 Å cannot be recognized from either single-energy plot, due to the high level of noise. By comparison, Fig. 20(c) shows the result of the small-window energy-extension process which uses Fig. 17(c) to determine R_β and Eq. (37) to form the image. We see that in Fig. 20(c), artifacts near the origin are mostly eliminated, resulting in a radial intensity plot with a single sharp peak with a FWHM of 0.56 Å.

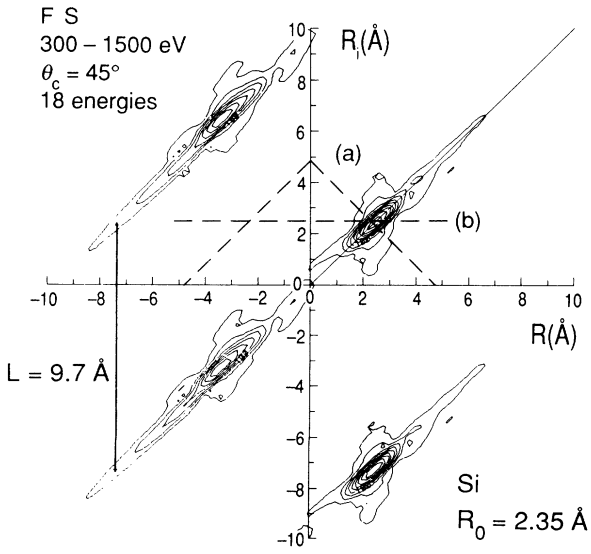

FIG. 19. $\Phi_{R_i}(R)$ for a diatomic Si system, with the Si-Si distance $R_\alpha=2.35$ Å. Evenly spaced wave numbers are used and the period is 9.7 Å.

VI. ACCURACY, PRECISION, AND HALF WIDTH OF THE RECONSTRUCTED IMAGE

In forming 3D images for direct viewing, there are three quantities to consider: The precision of $\mathbf{R}_\alpha$, the FWHM (or resolution) of the image, the accuracy of $\mathbf{R}_\alpha$ compared to the correct value. For multiple-energy image reconstruction in the backscattering geometry, we have shown that the integrals of Eq. (27) or Eq. (28) determine $\mathbf{R}_\alpha$. The integrals also cut through the high-intensity contours of $\Phi_{R_i}(R)$ at the narrowest cross section; the images produced thus have the smallest half-width in the emitter-scatterer direction. Either Eq. (27) or Eq. (28) generates 3D images whose resolution (i.e., FWHM) is also the precision of $\mathbf{R}_\alpha$.

The accuracy of $\mathbf{R}_\alpha$ in the backscattering geometry, however, is usually ≈ 0.3 Å. In the backscattering geometry, the optimal energies used for reconstruction are such that multiple scattering is strong even between

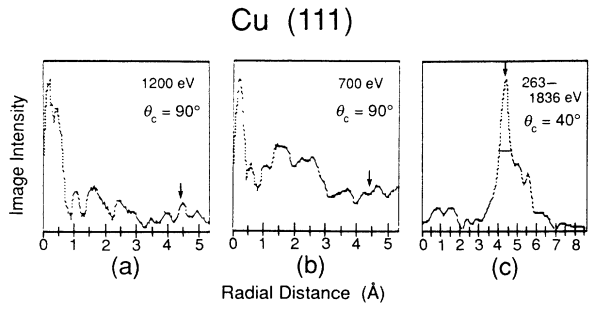

FIG. 20. Radial intensity plots along 19.5° from single-energy reconstruction [panels (a) and (b)] and the 14-energy SWEEP [panel (c)] for Cu(111); emitter at origin and scatterer position marked by arrows; FWHM marked by the horizontal bar in panel (c).

nearest-neighbor atoms. Hence, the scattering factor after multiple scattering depends on the crystal structure: $\{\mathbf{R}_1,\mathbf{R}_2,\ldots,\mathbf{R}_N\}$, where $\mathbf{R}_i$ are the atomic coordinates. The multiple-scattering renormalized scattering factor $t(\mathbf{k}_1,\mathbf{k}_2)$ is very different from the single scattering $f(\pi-\theta)$. Simple correction functions, like those defined in Eq. (32) or Eq. (35), are not expected to work. Without phase-shift correction, the accuracy of the image position is estimated to be ≈ 0.3 Å. A more serious problem is that in some materials the images may be split if energies between 100 and 350 eV are used. This splitting, however, is eliminated if a small angular window is used, as we have demonstrated in Fig. 11.

For multienergy reconstruction in the forward-scattering geometry, the orientation of $\hat{\mathbf{R}}_\alpha$ is determine in k-space by the focusing directions.[14–18] The bond distance R_α is found by the line $R_i=R$ of $\Phi^\alpha_{R_i}(R)$, examples are given in Figs. 15 and 17 and Ref. 7. These two steps define the precision of $\mathbf{R}_\alpha$. To form images for direct viewing, either Eq. (36) or Eq. (37) is used. In the examples given in this and previous works, the precision of $\mathbf{R}_\alpha$ is around ± 0.3 Å and the image FWHM is ≤ 1 Å. The accuracy of $\mathbf{R}_\alpha$ for the nearest-neighbor distance is good because at high energies, the scattering of near-neighbor atoms is dominated by the single-scattering factor $f(\theta)$. Therefore, the correction function based on single-scattering factors [Eq. (32) or Eq. (35)] works rather well.[5] In the forward-scattering geometry, the accuracy for the nearest-neighbor bond distance is estimated to be about the same as the precision, i.e., ≈ 0.3 Å. In using the focusing direction to determine the bond direction $\hat{\mathbf{R}}_\alpha$, there may be an error of $\delta\theta \simeq 3°-5°$. This translates to an error of $R_\alpha\delta\theta$ in the direction perpendicular to the bond: for a nearest-neighbor distance of $R_\alpha=2.5$ Å, this error is $\approx 0.1-0.2$ Å.

VII. USE OF UNIFORM Δk IN THE SWEEP

The energy range used in the SWEEP determines the quality of the FS curves shown in Figs. 15 and 17—hence, the precision of R_α improves with a larger energy range.[7,8] The FS image FWHM given by Eq. (17) or Eq. (18) also improves with a larger energy range. Similarly, in the BS geometry, the image width and resolution improve with a larger energy range according to Eq. (19) or Eq. (20). Therefore, it is advantageous to use the largest available energy range.

What about the number of energy points in a given interval and is there an optimal way of choosing these points? The answer is yes: whenever possible, choose energy points with a uniform wave-number interval. This choice produces a period $L=2\pi/(k_{i+1}-k_i)$ in the two-dimensional contour plot of $\Phi_{R_i}(R)$; i.e., $\Phi_{R_i+L}(r)=\Phi_{R_i}(R)$ (see, e.g., Fig. 19). The uniformly spaced k_n ensures that the exponential phase factor in Eq. (10) cancels out contributions from the different energy points in the space between periods. Therefore, high-intensity contours appear only at the predicted areas and artifacts are eliminated in the space between. The choice of a uniform Δk is more critical to backscattering than forward scattering. We shall discuss these scattering geometries separately.

In the forward-scattering geometry (e.g., Fig. 19), a uniform Δk produces high-intensity streaks with a period L.[7,8] In the intervals between $\Phi_{R_i}(R)$ and $\Phi_{R_i\pm L}(R)$, the intensities are canceled out by the energy sum. This produces very high-quality images along the cuts (a) or (b). If arbitrary energy points are used, it introduces artifacts at random places in $\Phi_{R_i}(R)$. This means artifacts could appear along the (a) or (b) cuts. A large period L implies

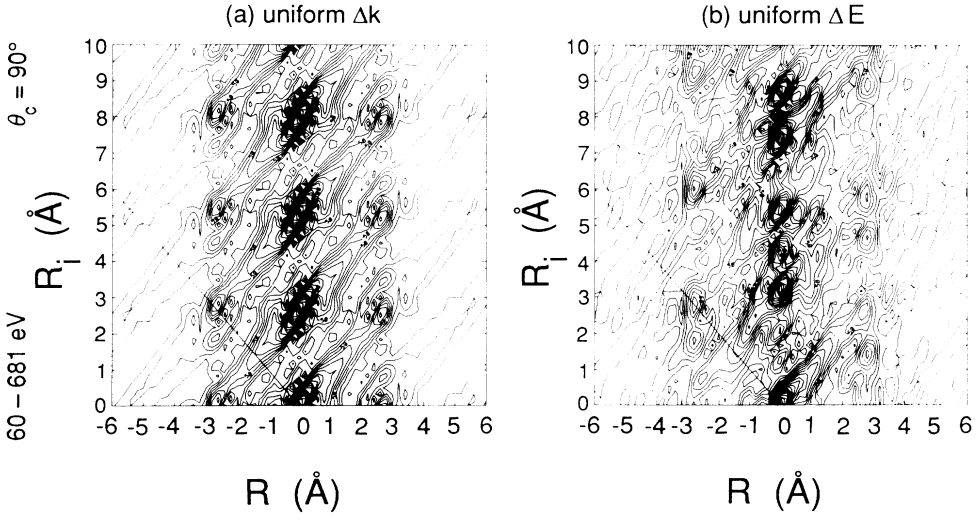

FIG. 21. Plot of $\Phi_{R_i}(R)$ for a diatomic Ni system: (a) uniform Δk with $L=2.7$ Å, (b) uniform ΔE with no period. High-intensity contours cutting across the $R_i=-R$ line constitute noise in the reconstructed image. Image position at $R=-2.52$ Å.

many energy points. In practice, it is desirable to at least eliminate random artifacts in the distance between the origin and R_α, the nearest-neighbor position. For this, the smallest periods are the following: For cut (a) in Fig. 19, $L_{\min} > 2R_\alpha$; for cut (b), $L_{\min} > R_\alpha$.

The intensity on the $R_i = R$ line in Fig. 19 is not critically dependent on a uniform Δk. Since the quality of this line defines the precision of R_α, it is acceptable to use energies with a nonuniform Δk in the forward-scattering geometry. However, it is important to avoid using energies that are not adequately spaced out in a given range—too many energies with similar wave numbers overemphasize a single phase factor and this leads to ineffective cancellation in Eq. (10).

In the backscattering geometry, it is critical that E_i are chosen with a uniform Δk and that the period L is large enough. This is because the atomic position is determined by the $R_i = -R$ line of $\Phi_{R_i}(R)$. We show in Fig. 21(a) a plot of $\Phi_{R_i}(R)$ for the diatomic Ni system considered in Fig. 3(c), except here, we only use five energy points in the range between 60 and 681 eV, with a uniform Δk. The period for this system is $L = 2.7$ Å. Furthermore, we have multiplied the square term in Eq. (4) by R_α^2, to simulate a stronger self-image term.[20] From Fig. 21(a), we see that the high-intensity contours of the self-image and image are streaked along 45°, as predicted by Fig. 2(a). With the very small period, the streaks cut across the $R_i = -R$ line, introducing significant artifacts to the image reconstruction. The situation is worse if a nonuniform Δk is used: Fig. 21(b) shows $\Phi_{R_i}(R)$ for the same energy range, but five energies with equal ΔE are used. The streaks from the self-image and image "periods" now cut across the $R_i = -R$ line at *random* R values. This causes a breakdown in the determination of R_α.

We now illustrate these principles by actual image reconstruction using Eq. (27) on the system considered before: Ni(001) (1×1)-Cu. In Fig. 22, the left panel is the same as that shown in Fig. 9; i.e., 17 energies in the range 60–681 eV are used, Δk is uniform, and the period $L = 10.7$ Å. The central panel uses five energies in the same range with a uniform Δk; the period is $L = 2.7$ Å. We note strong artifacts midway between the origin and image as well as just behind the image (inside the circle). Indeed, the two nearest-neighbor Ni images are almost entirely obscured by the artifacts. The right panel uses nine energies with a nonuniform Δk in the same energy range. With the amount of high-intensity random artifacts in the image ($-z$) half plane, it is not possible to determine where the real images are.

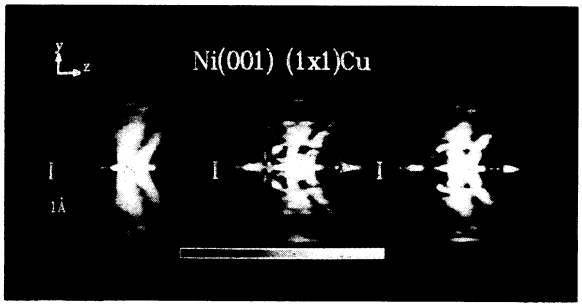

FIG. 22. Energy-extended image reconstruction. Left panel: same as that in Fig. 9, period $L = 10.7$ Å. Central panel: same as left panel, except period $L = 2.7$ Å. Right panel: same as left panel, except nine energies with a nonuniform Δk are used. Equation (27) is used in the image reconstruction for all three panels.

For energies chosen with a known period L, it is easy to determine the positions of the artifacts. Referring to Fig. 21(a), the artifacts of the self-image "periods" occur at $R = -L/2, -L$, etc., while those due to the image "periods" occur at $R = -R_\alpha + L/2$, $-R_\alpha + L/2$, $-R_\alpha + L/2$, etc. To properly image the nearest-neighbor atoms, it is desirable to keep the space between the origin and the image free from these artifacts. To achieve this, we need a period of at least $L > 2R_\alpha$. This choice ensures that the first bright spot measured from the origin is the true image. If we assume $R_\alpha \simeq 2.5$ Å, this means a period of $L \geq 6$ Å. Using an energy range of 60–320 eV, and an effective $\theta_c = 60°$, we obtain the following six energies for the backscattering geometry: 60, 96, 139, 191, 252, and 320 eV. Of course, reducing the wave-number interval Δk would further improve the image quality and reduce artifacts due to multiple scattering.

VIII. CONCLUSION

We have elucidated the fundamentals of energy extension in image reconstruction and illustrated these principles with multiple-scattering simulations. The advantages of using a small window in multiple-energy image reconstruction are demonstrated. Deep cusps in the backscattering factor cause split images and the splitting is removed by the small-window process. Examples are also given which demonstrate that (except for single-scattering systems) image reconstruction using holograms at single energies is unreliable. This makes the energy-extension process an important and necessary step of the technique.

In the forward-scattering geometry, a practical energy range is 200–1200 eV. This yields an image resolution of 0.4–0.6 Å by Eq. (17) or Eq. (18). In the backscattering geometry, an energy range of 60–350 eV yields an image resolution of 0.7–0.8 Å by Eq. (19) or Eq. (20). In the forward-scattering geometry, energy points with a uniform Δk are preferred, but not essential. In the backscattering geometry, it is critical to use energy points with a uniform Δk; this means special beam lines at synchrotron-radiation facilities are needed.

ACKNOWLEDGMENT

This work is supported in part by ONR Grant No. N00014-90-J-1749.

APPENDIX A: FULL WIDTH AT HALF MAXIMUM OF IMAGES

The Fourier transformations used in the energy-extension process involve numerical evaluations of the

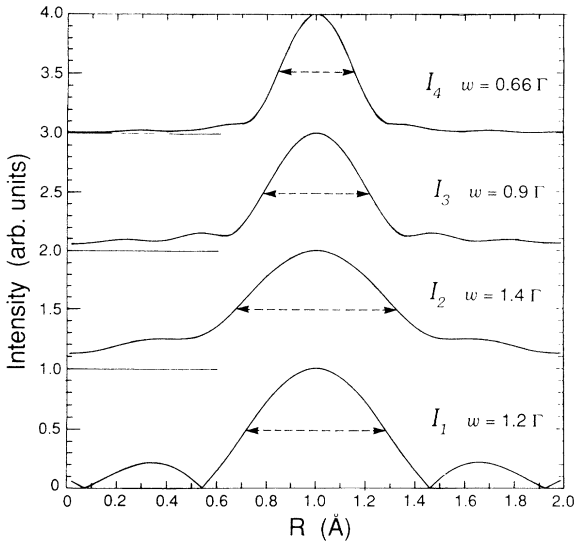

FIG. 23. The intensity vs R plots for the integrals defined in Eqs. (A1)–(A4) evaluated for the 263–1836-eV energy range. The w = FWHM indicated are averaged numerical widths over four different energy intervals.

following four integrals. We list these integrals below and express their numerical FWHM's as a function of $\Gamma = 2\pi/(k_{\max} - k_{\min})$. The numerical FWHM is obtained by averaging over the following four energy intervals: 60–300 eV, 60–452 eV, 60–681 eV, and 263–1836 eV. The integrals and their respective averaged w = FWHM's are

$$I_1(r) = \left| \int_{k_{\min}}^{k_{\max}} e^{-ikr} dk \right|, \quad w_1 = 1.2\Gamma , \tag{A1}$$

$$I_2(r) = \left| \int_{k_{\min}}^{k_{\max}} k^2 e^{-ikr} dk \right|, \quad w_2 = 1.4\Gamma , \tag{A2}$$

$$I_3(r) = \left| \int k e^{-i(kr/2)} \frac{\sin\frac{kr}{2}}{r/2} dk \right| , \quad w_3 = 0.9\Gamma , \tag{A3}$$

$$I_4(r) = \left| \int k e^{-i(3kr/2)} \frac{\sin\frac{kr}{2}}{r/2} dk \right| , \quad w_4 = 0.66\Gamma . \tag{A4}$$

In Eqs. (A1)–(A4), $r = (R_0 \mp R)$ and R_0 is the bond distance; the $-$ ($+$) sign corresponds to the forward-scattering (backscattering) geometry, respectively. The intensity plots of the four integrals and their averaged numerical widths are shown in Fig. 23 for $R_0 = \pm 1$ Å.

The integral

$$I_1 = \frac{\sin\left[(k_{\max} - k_{\min})\frac{r}{2}\right]}{r/2}$$

corresponds to the FWHM of a single-energy Fourier transformation. Its numerical width is more accurately given by 1.2Γ, instead of (the commonly used value) Γ.

The cut given by Eq. (17) corresponds to the integral [use $\theta_c \approx 0°$ and take the leading term in Eq. (10)]

$$I_a(r) = \left| \int_{k_{\min}}^{k_{\max}} k^2 e^{-2ikr} dk \right| , \tag{A5}$$

whose FWHM is half that of I_2, i.e., 0.7Γ. The cut given by Eq. (18) is simply I_3, with $w = 0.9\Gamma$. The cut given by Eq. (19) is also I_a [again, take the leading term in Eq. (10)], whose width is $w = 0.7\Gamma$. Finally, the cut given by Eq. (20) is I_4 [use Eq. (13)] with width $w = 0.66\Gamma$.

Comparing the single-energy width $w_1 = 1.2\Gamma$ to the *full-window* energy-extended width of Eq. (20), i.e., $w_4 = 0.66\Gamma$, the latter is much narrower if the wave-number range $(k_{\max} - k_{\min})$ is the same as the single-energy's wave number. Using the largest energy in an energy range, the single-energy width is $w_1 = 1.2\Gamma = 2.4\pi/k_{\max}$. The full-window energy-extended width w_4 is narrower than w_1 if $1.3\pi/(k_{\max} - k_{\min}) < 2.4\pi/k_{\max}$ or $k_{\min} < 0.45 k_{\max}$. This is the condition for improving the image resolution by energy extension if a full window is in effect.

APPENDIX B: SCATTERING FACTOR INDUCED IMAGE SPLITTING

In the backscattering geometry, the scattering factor often has sharp cusps at which angles its phase goes through a π change[22] (see Fig. 4). We can divide the Fourier transformation into separate regions at these cusps:

$$I(R) = \left| \int_{\Omega} \chi(\mathbf{k}) e^{i\mathbf{k}\cdot\mathbf{R}} k^2 d\Omega \right| \tag{B1}$$

$$= \left| \int_{\Omega_1} \chi_1(\mathbf{k}) e^{i\mathbf{k}\cdot\mathbf{R}} k^2 d\Omega_1 + e^{i\pi} \int_{\Omega_2} \chi_2(\mathbf{k}) e^{i\mathbf{k}\cdot\mathbf{R}} k^2 d\Omega_2 \right| , \tag{B2}$$

where Ω is the full hemispherical window, Ω_1 and Ω_2 are small windows, and the phase $e^{i\pi}$ is from the π jump of the scattering factor at a cusp. The integrals over $d\Omega_1$ and $d\Omega_2$ produce real-space functions shifted from each other; this is due, in part, to the different slopes in the phases of the scattering factors in the two regions. Thus, we have

$$I(R) \approx |A(R) - B(R)| = [|A(R)|^2 + |B(R)|^2 - 2|A(R)|\,|B(R)|\cos\phi]^{1/2} . \tag{B3}$$

The image position $I(R)$ goes through a sharp minimum at $\phi \approx 0$, causing the image peak to be split.

[1] A. Szoeke, in *Short Wavelength Coherent Radiation: Generation and Applications,* edited by D. T. Attwood and J. Boker, AIP Conf. Proc. No. 147 (AIP, New York, 1986).
[2] J. J. Barton, Phys. Rev. Lett. **61**, 1345 (1988).
[3] G. R. Harp, D. K. Saldin, and B. P. Tonner, Phys. Rev. Lett. **65**, 1012 (1990).
[4] C. M. Wei, T. C. Zhao, and S. Y. Tong, Phys. Rev. Lett. **65**, 2278 (1990).

[5]S. Y. Tong, C. M. Wei, T. C. Zhao, H. Huang, and Hua Li, Phys. Rev. Lett. **66**, 60 (1991).

[6]C. M. Wei, T. C. Zhao, and S. Y. Tong, Phys. Rev. B **43**, 6354 (1991).

[7]H. Huang, Hua Li, and S. Y. Tong, Phys. Rev. B **44**, 3240 (1991).

[8]S. Y. Tong, H. Huang, and Hua Li, in *Advances in Surface and Thin Film Diffraction,* edited by T. C. Huang, P. I. Cohen, and D. J. Eaglesham, MRS Symposia Proceedings No. 208 (Materials Research Society, Pittsburgh, 1991), p. 13; S. Y. Tong, Hua Li, and H. Huang, Phys. Rev. Lett. **67**, 3102 (1991).

[9]S. Hardcastle, Z. L. Han, G. R. Harp, B. L. Chen, D. K. Saldin, and B. P. Tonner, Surf. Sci. Lett. **245**, L190 (1991).

[10]B. P. Tonner, Z. L Han, G. R. Harp, and D. K. Saldin, Phys. Rev. B **43**, 14423 (1991).

[11]Peijun Hu and D. A. King, Nature **353** (1991); Peijun Hu, C. J. Barnes, and D. A. King, Chem. Phys. Lett. **183**, 521 (1991).

[12]D. K. Saldin and P. L. de Andres, Phys. Rev. Lett. **64**, 1270 (1990).

[13]J. J. Barton and L. J. Terminello, in *The Structure of Surfaces–III,* edited by S. Y. Tong, M. A. Van Hove, X. Xie, and K. Takayanagi (Springer, Berlin, 1991).

[14]H. C. Poon and S. Y. Tong, Phys. Rev. B **30**, 6211 (1984); S. Y. Tong, H. C. Poon, and D. R. Snider, *ibid.* **32**, 2096 (1985); M. L. Xu and M. A. Van Hove, Surf. Sci. **207**, 215 (1989).

[15]W. F. Egelhoff, Jr., Phys. Rev. Lett. **59**, 559 (1987).

[16]S. A. Chambers, in *Advances in Physics,* edited by S. Doniach (Taylor and Francis, London, 1991).

[17]S. Y. Tong, M. W. Puga, H. C. Poon, and M. L. Xu, in *Chemistry and Physics of Solid Surfaces VI,* edited by R. Vanselow and R. Howe (Springer, New York, 1986).

[18]C. S. Fadley, in *Synchrotron Radiation Research: Advances in Surface Science,* edited by R. Z. Bachrach (Plenum, New York, 1990).

[19]H. C. Poon, D. Snider, and S. Y. Tong, Phys. Rev. B **33**, 2198 (1986).

[20]S. Thevuthasan, G. S. Herman, A. P. Kaduwela, R. S. Saiki, Y. J. Kim, and C. S. Fadley, Phys. Rev. Lett. **67**, 469 (1991).

[21]D. K. Saldin, G. R. Harp, B. L. Chen, and B. P. Tonner, Phys. Rev. B **44**, 2480 (1991).

[22]J. J. Barton, S. W. Robey, C. C. Bahr, and D. A. Shirley, in *The Structure of Surfaces,* edited by M. A. Van Hove and S. Y. Tong (Springer, Heidelberg, 1985), p. 191. See also, J. G. Tobin, M. K. Wagner, X. Q. Guo, and S. Y. Tong, in *Advances in Surface and Thin Film Diffraction* (Ref. 8), p. 283, Fig. 9.

[23]S. Y. Tong and C. H. Li, in *Critical Reviews in Solid State and Materials Sciences,* edited by D. E. Schuele and R. W. Hoffman (CRC, Cleveland, 1981), Vol. 10, p. 209.

[24]S. Y. Tong, C. H. Li, and A. R. Lubinsky, Phys. Rev. Lett. **39**, 498 (1977).

[25]C. H. Li, A. R. Lubinsky, and S. Y. Tong, Phys. Rev. B **17**, 3128 (1978).

[26]J. J. Rehr and R. C. Albers, Phys. Rev. B **41**, 8139 (1990).

[27]G. R. Harp (private communication).

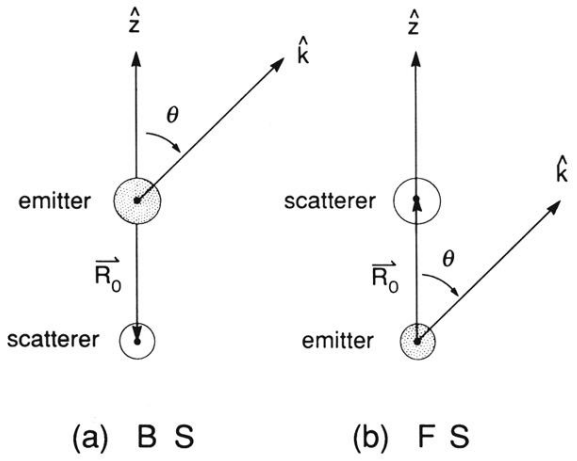

FIG. 1. Schematic diagram of emitter-scatterer system for (a) backscattering and (b) forward-scattering geometries.

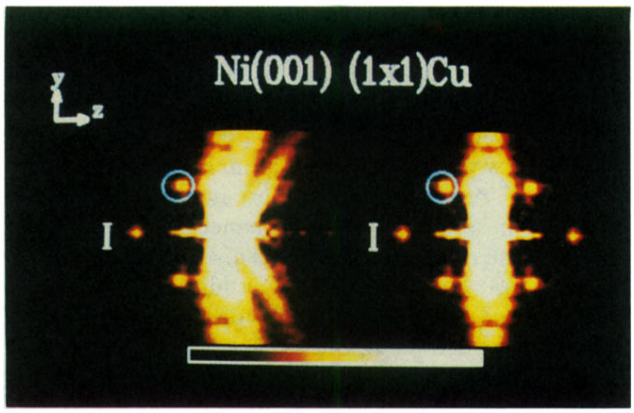

FIG. 10. Full-window ($\theta_c = 90°$) energy-extended image reconstruction. Left panel: Same as that in Fig. 9. Right panel: Cut normal to surface; Eq. (28) is used in the image reconstruction process. Vertical bar indicates 1 Å.

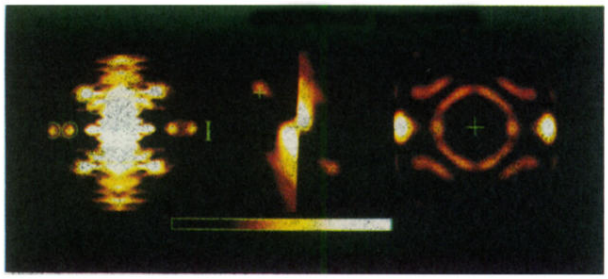

FIG. 11. **Left panel:** Full-window ($\theta_c = 90°$) energy-extended image reconstruction using the 60–286-eV energy range. Other conditions same as those in Fig. 10, right panel. Split images enclosed by circles. Center: Small-window ($\theta_c = 45°$) energy-extended nearest-neighbor image. Crosses mark emitter and scatterer positions. Right: Small-window ($\theta_c = 30°$) energy-extended image of Ni atom below emitter. Crosses mark emitter and scatterer positions. The twin images appear on the right halves of each panel.

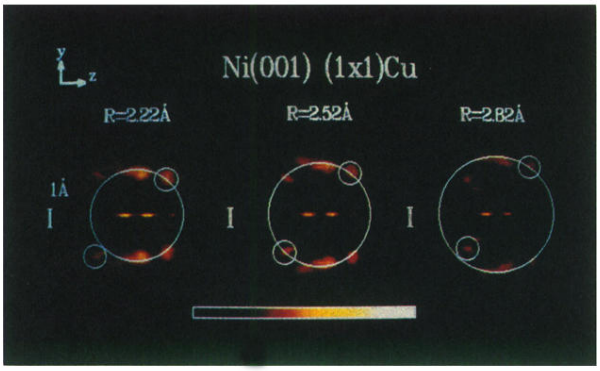

FIG. 12. Full-window ($\theta_c = 90°$) energy-extended image reconstruction using different trial values of R_i for the nearest-neighbor Ni atom. The separation between the self-image (at the one o'clock position) and image (at the seven o'clock position) remains constant.

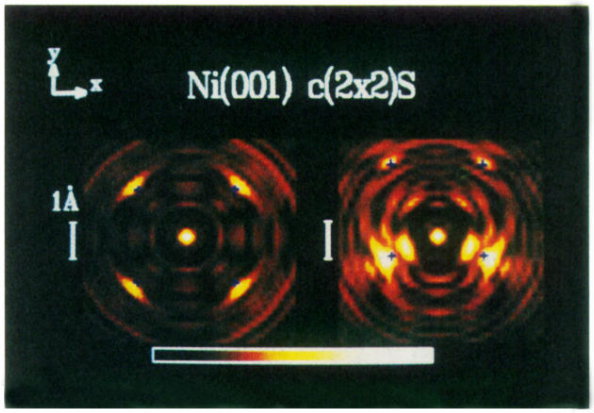

FIG. 14. Full-window ($\theta_c = 90°$) energy-extended image reconstruction for *S* at the symmetric fourfold site (left panel) and the asymmetric site (right panel).

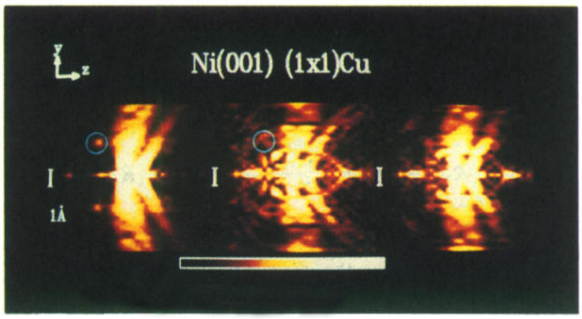

FIG. 22. Energy-extended image reconstruction. Left panel: same as that in Fig. 9, period $L = 10.7$ Å. Central panel: same as left panel, except period $L = 2.7$ Å. Right panel: same as left panel, except nine energies with a nonuniform Δk are used. Equation (27) is used in the image reconstruction for all three panels.

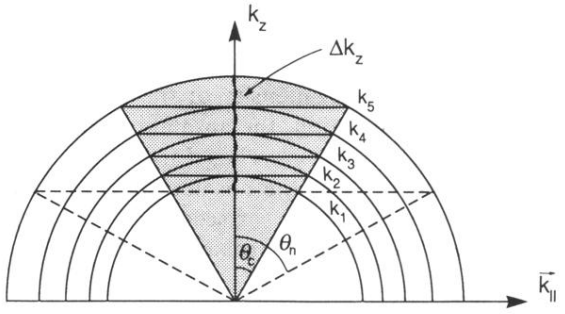

FIG. 7. Illustration of Δk_z extension (wiggly line) for a small-window $\theta_c < \pi/2$. The angular window is enlarged to θ_n after the 5 energy extensions.

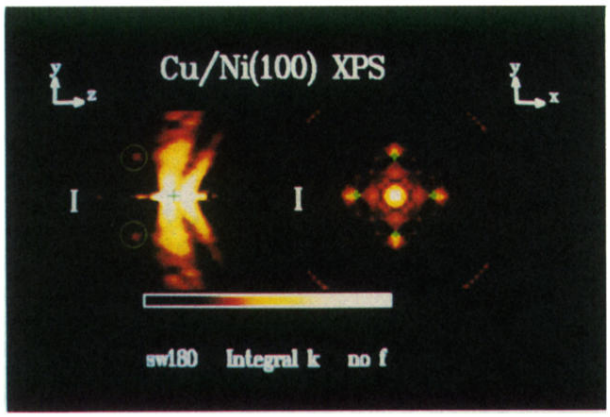

FIG. 9. Full-window ($\theta_c = 90°$) energy-extended image reconstruction using Eq. (27). Left panel: Cut normal to surface. Right panel: Cut parallel to surface. Vertical bar indicates 1 Å.